A tumor-promoting inflammatory *SPP1*$^{+}$ macrophage—IL-6—CRP axis drives immune dysfunction in bladder cancer

Michelle A. Tran [a,b #], Byuri Angela Cho [b,c,d #], Sudeh Izadmehr [a#], Seong-Keun Yoo [b,c,e #], Dina Youssef [a,b], Jonathan F. Anker [a,b], Adam M. Farkas [a,b], Igor Figueiredo [b], Karen Lee [a,b], Aparna Ananthanarayanan [a,b], Sreekumar Balan [a,b], Sayali Onkar [a,b], Romain Banchereau [f], Saurabh Gupta [g], Aparna Chhibber [g], Li Wang [a], Kristin G. Beaumont [h], Ziao Li [a], Monica Garcia-Barros [i], Mesude Bicak [a], Carlos Cordon-Cardo [i], Rachel Brody [i], Seunghee Kim-Schulze [b], Kobe Yuen [f], Sanjeev Mariathasan [f], Saad O. Atiq [a], Tolulope T. Adeyelu [j], Andrew Elliott [j], Pedro Barata [k], Rana R. McKay [l], Sacha Gnjatic [a,b], Edgar Gonzalez-Kozlova [b], Reza Mehrazin [m], Amir Horowitz [b,c], John P. Sfakianos [m], Diego Chowell [b,c†], Matthew D. Galsky [a†], Nina Bhardwaj [a,b,j †]

[a] *Division of Hematology and Medical Oncology, Tisch Cancer Institute, Icahn School of Medicine at Mount Sinai, New York, NY, USA*
[b] *Department of Immunology & Immunotherapy, The Marc and Jennifer Lipschultz Precision Immunology Institute, Icahn School of Medicine at Mount Sinai, New York, NY, USA*
[c] *Department of Oncological Sciences, Tisch Cancer Institute, Icahn School of Medicine at Mount Sinai, New York, NY, USA.*
[d] Present address: *Genomic Medicine Institute, Medical Research Center, Seoul National University, Seoul, Republic of Korea*
[e] Present address: *Samsung Precision Genome Medicine Institute, Samsung Medical Center, Sungkyunkwan University School of Medicine, Seoul, Republic of Korea*
[f] *Genentech, San Francisco, CA, USA*
[g] *Bristol Myers Squibb, Princeton, NJ, USA*
[h] *Department of Genomics, Icahn School of Medicine at Mount Sinai, New York, NY, USA*
[i] *Department of Pathology, Icahn School of Medicine at Mount Sinai, New York, NY, USA*
[j] *Caris Life Sciences, Irving, TX, USA*
[k] *Seidman Cancer Center, University Hospitals, Cleveland, OH, USA*
[l] *Moores Cancer Center, University of California San Diego, San Diego, CA, USA*
[m] *Department of Urology, Icahn School of Medicine at Mount Sinai, New York, NY, USA*

[#, †] These authors contributed equally to this work.

Addresses for correspondence:
Dr. Diego Chowell, Ph.D.
The Tisch Cancer Institute
Icahn School of Medicine at Mount Sinai
1 Gustave Levy
New York, NY 10029
diego.chowell@mssm.edu
Twitter/X: @DiegoChowell

Dr. Matthew D. Galsky, M.D.
Division of Hematology and Medical Oncology
Icahn School of Medicine at Mount Sinai
1 Gustave Levy
New York, NY 10029
Matthew.galsky@mssm.edu

Dr. Nina Bhardwaj, M.D., Ph.D.

The Tisch Cancer Institute
Icahn School of Medicine at Mount Sinai
1 Gustave Levy
New York, NY 10029
nina.bhardwaj@mssm.edu
Twitter/X: @BhardwajLab

Running Title: An *SPP1*$^{+}$ Macrophage—IL-6—CRP Axis in Bladder Cancer

Declaration of Interests:

SKY, BAC, and DC have a provisional patent application for using routine blood tests and clinical variables to predict cancer immunotherapy response. TA and AE report Employment and Stock with Caris Life Sciences. PB reports grants or personal fees from Astellas, AstraZeneca, AVEO Oncology, Bayer, BMS, Dendreon, Eisai, EMD Serono, ESSA Pharma, Guardant Health, Ipsen, Caris Life Sciences, Exelixis, Janssen, Merck, Merus, MJH, Myovant, Novartis, Pfizer, Seattle Genetics, Syncromune, and UroToday. RRM is an advisor or consultant for Ambrx; Arcus Biosciences, Inc.; AstraZeneca; AVEO Pharmaceuticals, Inc.; Bayer; Blue Earth Diagnostics; Bristol Myers Squibb (BMS); Calithera Biosciences, Inc.; Caris Life Sciences; Daiichi Sankyo, Inc.; Dendreon Pharmaceuticals LLC; Exelixis; Johnson & Johnson ; Lilly; Merck & Co., Inc.; Myovant Sciences; Neomorph; Nimbus Therapeutics; Novartis Pharmaceuticals Corporation; Pfizer Inc.; Sanofi; Seagen Inc.; Sorrento Therapeutics, Inc.; Telix Pharmaceuticals; and Tempus. RRM receives institutional research funding from Artera AI, AstraZeneca, Bayer, BMS, Exelixis, Oncternal Therapeutics, and Tempus. SG reports grant funding from Regeneron, Boehringer-Ingelheim, Genentech, Takeda, BMS/Celgene, and personal fees from Taiho Pharmaceuticals, outside the submitted work; in addition, SG has a patent for Multiplex immunohistochemistry (MICSSS) currently unlicensed. AH receives research funding from Astra Zeneca and has served on advisory boards for Purple Biotech and UroGen. JPS reports consultancy in Pacific Edge, Natera, and Merck. MDG reports consultancy in BioMotiv, Janssen, Astellas, Pfizer, EMD, Serono, Seattle Genetics, Inctye, Dracen, Inovio, Aileron, and Dragonfly and grants from Dendreon, Novartis, Merck, Genentech, Bristol Myers Squibb, and AstraZeneca. NB receives

research support from Merck, Parker Insitute for Cancer Immunotherapy and is a consultant, advisor, or board member for Apricity, BreakBio, Epitopea, Genentech, Genotwin, Primevax, and Tempest Therapeutics.

Abstract:

Immune checkpoint blockade (ICB) has revolutionized treatment for urothelial bladder cancer (UC), yet response rates remain limited. Inflammation promotes disease progression and treatment resistance, with macrophages shaping the tumor microenvironment (TME). While elevated blood C-reactive protein (CRP) associates with poor clinical outcomes in UC, its relationship to the TME remains unclear. Here, we show that elevated plasma IL-6 and CRP associate with increased tumor macrophage infiltration across multiple ICB-treated cohorts. Single-cell RNA sequencing of the largest UC atlas to date, integrated with bulk RNA sequencing, identifies enrichment of immunosuppressive *SPP1*$^{+}$ macrophages in TMEs from patients with high plasma IL-6. Spatial and functional analyses demonstrate that *SPP1*$^{+}$ macrophages suppress T cell activity partly via IL-6 signaling, whereas *CXCL9*$^{+}$ macrophages promote T cell activation. These findings link systemic inflammation to local immune dysfunction and define a macrophage-driven axis associated with ICB resistance and therapeutic targets to improve immunotherapy outcomes in UC.

Statement of Significance:

Single-cell and bulk RNA sequencing, spatial analyses, and functional experiments identify opposing *SPP1*$^{+}$ and *CXCL9*$^{+}$ macrophage programs regulate T-cell function and immune checkpoint blockade therapy response in bladder cancer. Elevated plasma CRP and IL-6 mark *SPP1*$^{+}$ macrophage–driven immune suppression, defining a targetable IL-1β/IL-6 axis that contributes to immunotherapy resistance.

Main Text:

Introduction:

Immune checkpoint blockade (ICB) has revolutionized the cancer treatment landscape of urothelial cancer of the bladder (UC)(1). Anti-programmed death 1 (PD-1)/programmed death-ligand 1 (PD-L1) ICB therapies can induce durable clinical responses in patients with UC, even in the metastatic setting. However, only a minority of patients with UC respond to ICB(2–10). These observations have prompted studies seeking to understand the immunobiological mechanisms underlying intrinsic ICB resistance to identify new combinatorial strategies to extend the benefits of ICB to a large population of patients with UC.

Tumor-promoting inflammation is a well-established hallmark of cancer pathogenesis, playing a crucial role in disease aggressiveness and treatment resistance across various tumor types(11). This inflammatory state within the tumor microenvironment (TME) is characterized by the presence and interplay of diverse immune and stromal cells, including tumor-associated macrophages (Macs). These cells contribute to the inflammatory milieu through the production of a variety of cytokines, chemokines, growth factors, and other signaling molecules that support tumor growth, metastasis, and evasion of antitumor immunity. Indeed, we previously demonstrated that two gene signatures derived from bulk RNA sequencing (RNA-seq) data, reflecting the balance to adaptive immunity and tumor-promoting inflammation, were highly correlated with objective response rate and survival with ICB treatment among cohorts of patients with UC(12). While significant progress has been made in understanding the mechanisms of tumor-promoting inflammation in model systems, the cellular and molecular events that underlie tumor-promoting inflammation in human tumors remain poorly defined.

Some of the strongest evidence linking tumor-promoting inflammation to clinical outcomes in cancer patients comes from studies examining plasma C-reactive protein (CRP). CRP, an annular pentameric protein produced by the liver in response to inflammatory cytokines, particularly interleukin-6 (IL-6), has consistently emerged as a powerful prognostic

indicator(13,14). Numerous studies have correlated elevated plasma CRP levels with poor outcomes across a spectrum of cancer types, specifically in patients with UC and treated with ICB(13,14). Despite the longstanding and consistent relationship between CRP and poor outcomes in patients with cancer, to our knowledge, no prior studies have comprehensively explored the connection between this inflammatory biomarker and features of the TME. Understanding these relationships could potentially reveal new targets for therapeutic intervention.

Here, we sought to define the features of the UC TME underlying tumor-promoting inflammation and their role in the evasion of antitumor immunity **(Figure 1)**. Utilizing clinical trial cohorts, we first bolstered the evidence that elevated CRP is associated with poor outcomes in patients with metastatic UC (mUC) regardless of treatment. We subsequently demonstrated that on-treatment decline of CRP is associated with improved outcomes with ICB, but not with chemotherapy, suggesting (a) potentially therapeutically modifiable biology associated with elevated CRP and (b) that the manner in which the TME is modulated to yield declines in CRP has distinct clinical implications. We then showed that IL-6 in the plasma, known to regulate CRP production by hepatocytes, was highly correlated with plasma CRP across multiple clinical trial cohorts, and was also associated with ICB outcomes. Deconvolution of bulk RNA-seq data revealed that UC TMEs associated with increased plasma CRP were enriched in Mac infiltration. We therefore characterized the landscape of myeloid cells in the largest single cell RNA-seq (scRNA-seq) atlas of UC to date, further revealing enrichment of *SPP1*$^{+}$ and *NLRP3*$^{+}$ Macs in TMEs associated with increased plasma CRP. Consistent with data in other tumor types, we identified a duality of pro-inflammatory *SPP1*$^{+}$ Macs associated with tumor-promoting transcriptional programs and *CXCL9*$^{+}$ Macs associated with antigen presentation-related transcriptional programs. Integrated analyses of circulating analytes, spatial transcriptomics, and functional assays revealed axes linking *SPP1*$^{+}$ Macs to suppressed T cell immunity, in contrast to *CXCL9*$^{+}$ Macs, which have been associated with enhanced CXCR3^{+} T cell and NK cell tumor

infiltration, proliferation, and anti-tumor cytotoxicity(15–17). Experimental data revealed that *SPP1*$^{+}$ Macs impaired T cell function, at least in part, through IL-6 signaling. Overall, our study identifies diverse Mac states in the UC TME and reveals a duality of transcriptional programs that could guide therapeutic modulation in UC.

Results:

Elevated plasma CRP is associated with poor outcomes in patients with advanced UC

We previously demonstrated through bulk RNA-seq that UC TMEs with a stronger tumor-promoting inflammatory profile are linked to poorer outcomes to ICB therapy, which has now been externally validated by an independent group in a real-world cohort comprising >6000 patients(12,18). To examine the relationship between plasma CRP and outcomes in patients with mUC treated with ICB or chemotherapy, we analyzed data from four large clinical trial cohorts: IMvigor210(2,19), IMvigor211(20), IMvigor130(21), and HCRN GU14-182(22) (**Figures 1 and S1A-D**).

IMvigor210 was a phase 2 trial consisting of two cohorts that evaluated PD-L1 blockade with atezolizumab in patients with mUC. IMvigor210 cohort 1 comprised first-line, cisplatin-ineligible patients with metastatic disease, whereas cohort 2 included second-line, post-platinum chemotherapy patients with metastatic disease. IMvigor211 was a phase 3 trial randomizing patients with mUC with disease progression despite prior platinum-based chemotherapy to atezolizumab versus chemotherapy with a taxane or vinflunine. IMvigor130 was a partially blinded, randomized controlled phase 3 study comparing atezolizumab plus platinum-based chemotherapy, atezolizumab alone, or placebo plus platinum-based chemotherapy in patients with previously untreated locally advanced or mUC. HCRN GU14-182 was a phase 2 trial of pembrolizumab versus placebo as switch maintenance treatment in patients with mUC achieving at least stable disease on first-line platinum-based chemotherapy; patients randomized to placebo could cross-over to receive pembrolizumab at the time of disease progression.

Elevated pre-treatment plasma CRP levels were significantly correlated with reduced overall survival (OS) for patients treated with atezolizumab across both cohorts of IMvigor210 (**Figure 2A**). In multivariable Cox proportional hazards regression models examining CRP quartiles and OS, higher CRP was significantly associated with reduced survival after adjusting for previously reported ICB predictors(23) (**Figures S2A-C**). Overall, higher baseline plasma CRP levels were linked to significantly worse OS in patients receiving either ICB or chemotherapy in the IMvigor211, IMvigor130, and HCRN GU14-182 studies (**Figure 2A**). Collectively, these results underscore that plasma CRP, an easily accessible and routinely measured analyte in clinical practice, is associated with poorer prognosis in patients with mUC treated with either ICB or chemotherapy, with similar trends seen when objective response rate was used as an outcome measure (**Figure S3A**).

Though we found that elevated pre-treatment CRP levels correlated with poor outcomes in patients with UC receiving either ICB or chemotherapy, we hypothesized that the on-treatment modulation of CRP might have distinct immunological and clinical implications depending on the therapeutic approach. Thus, we next assessed the relationship between on-treatment CRP changes and OS across these studies. Patients who experienced a reduction in plasma CRP during ICB treatment had significantly improved OS relative to those who did not; however, this association was not observed in patients treated with chemotherapy alone (**Figure 2B**). Likewise, these findings were replicated across trials when objective response rate was used as the clinical outcome measure (**Figure S3B**). The association between on-treatment CRP reduction and improved survival with ICB but not chemotherapy raises the possibility that: (a) the inflammatory processes responsible for elevated CRP levels in the bloodstream may be therapeutically modifiable, and (b) treatment-specific CRP dynamics could reflect distinct alterations within the TME.

IL-6 correlates with CRP and is also associated with poor prognosis in mUC

Previous research has demonstrated that hepatocytes are the primary source of circulating CRP, with their production tightly regulated by inflammatory cytokines, most notably IL-6(24,25). In cardiovascular disease, where CRP is used routinely as a biomarker of risk, Mendelian randomization studies have demonstrated that CRP is not causally related to atherogenesis, whereas “upstream” inflammatory cytokine networks involving local production of interleukin 1 beta (IL-1β) and IL-6 have been more directly implicated(26,27). To explore the relationship between plasma CRP and plasma cytokines/chemokines in mUC, we analyzed the correlations between levels of baseline CRP and 92 plasma immune-related analytes using O-link data from the HCRN GU14-182 cohort (**Figures 3A and B**). Among these, 46 analytes exhibited significant positive correlations with CRP, with IL-6 showing the strongest correlation (Pearson’s $r = 0.79$; $p < 0.0001$), as has been well established(28,29). This was followed by colony stimulating factor 1 (CSF-1), also known as macrophage colony stimulating factor (M-CSF) (Pearson’s $r = 0.59$; $p < 0.0001$), a cytokine known to promote the survival of Macs(30). Interestingly, we found both plasma IL-6 and CSF-1 to be significantly elevated in patients with UC as compared to age-matched healthy donors (HDs**; Figures S4A and B**). Importantly, we observed that IL-6 elevation and the positive IL-6—CRP correlation were present in non-muscle invasive bladder cancer (NMIBC) and muscle invasive bladder cancer (MIBC) patients with only primary tumors and no metastatic disease, indicating that these systemic cytokine changes reflect core features of UC biology rather than merely metastatic burden **(Figure S4C and D)**.

A strong positive correlation between baseline CRP and IL-6 was also observed in the IMvigor210 trial (Pearson’s $r = 0.76$; $p < 0.0001$; **Figure 3C**). To probe the features of the UC TME linked with high versus low plasma IL-6, we subsequently compared matched bulk RNA-seq data from the pre-ICB tumors of patients with the highest (Q4) and lowest quartile (Q1) values of plasma IL-6 from the IMvigor210 trial(31). Notable differentially expressed genes (DEGs) in tumors in the IL-6 Q4 versus Q1 group included genes associated with myeloid cells and inflammatory cytokines (e.g., *SPP1, IL1B, IL1RAP, CXCL8, TREM1,* and *CLEC5A*) as well as

basal-squamous bladder cancer (e.g., *CD44, KRT5, KRT6, KRT14, CDH3,* and *EGFR*; **Figure 3D**). Gene set overrepresentation analysis (GSOA) of DEGs revealed up-regulation of numerous immune-related and hypoxia signaling pathways in the IL-6 Q4 group (**Figure 3E**). When stratifying tumors in the IMvigor210 trial by TCGA bladder cancer subtype(32), we found that patients with the highest quartile of plasma IL-6 levels had a higher prevalence of basal-squamous subtype tumors (χ^2 test $p = 0.002$; **Figure 3F**). Together, these findings reveal that (a) plasma IL-6 and CRP are highly correlated, consistent with the established role of IL-6 in stimulating CRP production from hepatocytes, and (b) UC TMEs linked to elevated plasma IL-6 are enriched in programs related to tumor-promoting inflammation, myeloid cells, and basal-squamous UC cells.

Using a binary cut-point, increased plasma IL-6 has previously been correlated with poor outcomes in IMvigor210(33). We confirmed a "dose-dependent" inverse relationship between plasma IL-6 and OS in the IMvigor210 cohort upon segregating patients into quartiles by plasma IL-6 levels (log-rank test $p < 0.0001$; **Figure 3G**). HCRN GU14-182 also displayed significant differences in OS based on IL-6 levels, with patients with high IL-6 (Q4) demonstrating significantly worse OS compared to those with lower IL-6 level groups (log-rank test $p < 0.0001$; **Figure 3H**). A dose-dependent inverse relationship between CSF-1 and OS was also observed in HCRN GU14-182 (log-rank test $p = 0.0002$; **Figure S4E**).

We turned to RNAscope, an *in situ* hybridization technique known for its high sensitivity and specificity in detecting RNA molecules, to better identify the source of plasma IL-6 (**Figure 3I**). Applying RNAscope and subsequent HALO whole-slide digital analysis to baseline samples from the HCRN GU14-182 cohort (n = 10), we observed that *IL6* mRNA expression in the TME was positively correlated with plasma CRP (Pearson's $r = 0.81$, $p = 0.009$; **Figure 3J**) and plasma IL-6 protein (Pearson's $r = 0.85$, $p = 0.004$; **Figure 3K**). Additionally, from studying a total of 2,432,085 cells, we found that *IL6* mRNA was found to be produced more abundantly from immune and stromal regions versus tumor regions (Mann–Whitney *U* test $p = 0.004$; **Figure 3L**).

Multi-transcriptomic profiling of SPP1^{+} *and* CXCL9^{+} *Macs in UC*

Given our findings linking plasma analytes associated with tumor-promoting inflammation (e.g., CRP and IL-6) with poor outcomes in UC, and bulk RNA-seq data suggesting distinct TMEs underlying these plasma analytes, we sought to profile the cellular landscape of UC at high resolution. We conducted scRNA-seq on 42 bladder tumor samples from Mount Sinai School of Medicine (MSSM), extending our prior single-cell profiling efforts(34–36) with an expanded tumor cohort, including 10 tumors from a trial exploring neoadjuvant pembrolizumab in MIBC (HCRN GU20-444; ClinicalTrials.gov identifier: NCT05406713). scRNA-seq was performed on freshly dissociated UC tissue derived from transurethral resection of bladder tumor (TURBT) or cystectomy specimens. We analyzed these dissociated tumor cells using droplet-based scRNA-seq (10X Genomics)(37) and integrated the data from these 42 tumors with 8 additional tumors from a publicly available UC scRNA-seq dataset(38), creating the largest UC scRNA-seq atlas to date. The clinical characteristics of this combined cohort are detailed in **Table S1**. In total, this atlas encompassed 50 unique tumors, including 15 NMIBC tumors and 35 MIBC tumors. The majority of these tumors were naïve to systemic ICB therapy (82%, 41/50). The atlas also contained matched normal-adjacent tissue from cystectomy specimens for six patients (5 MIBC, 1 NMIBC).

scRNA-seq analysis of these 56 samples identified a total of 41 distinct cell types; 40 were annotated using label transfer based on our previous study(39), while neutrophils were additionally defined (**Figures 4A and S5A-D**). The immune cell clusters were not patient-specific, indicating shared biology (**Figure S5B**). We next leveraged the marker genes for each cell type from our integrated scRNA-seq data to deconvolute cellular composition of the UC TME associated with high versus low plasma IL-6 using the bulk RNA-seq data from the IMvigor210 study (**Figure 4B**). This analysis revealed an enrichment of *SPP1*$^{+}$ Macs as well as *NLRP3*$^{+}$ Macs, neutrophil, and basal-like tumor cells in patients with high plasma IL-6 levels. Consistent with

previous reports[14,26], the Mac subsets we identified in our scRNA-seq analysis did not align with traditional M1/M2 gene signatures[21], reinforcing the notion that Mac heterogeneity in the human TME extends beyond the M1/M2 polarization framework (**Figures S5E and F**).

As *SPP1*$^+$ Macs have been reported to underlie treatment resistance and poor outcomes in other cancers, and the two-gene ratio of *SPP1*:*CXCL9* has been recently developed as a simple surrogate for distinguishing tumor-promoting versus anti-tumor Mac polarization in the TME(17,40–43), we focused further attention on the *SPP1*$^+$ and *CXCL9*$^+$ Mac populations in the UC TME. We quantified the number of Macs expressing *SPP1* or *CXCL9* independently, as well as those co-expressing both genes (**Figure 4C**). We observed that most Macs expressed either *SPP1* or *CXCL9* in a mutually exclusive manner, with Macs co-expressing both genes constituting the smallest proportion. To characterize their biological characteristics, we then identified DEGs of *SPP1*$^+$ Macs versus *CXCL9*$^+$ Macs and performed GSOA based on Hallmark gene sets(44) (**Figures 4D and E; Table S2**). Notably, *SPP1*$^+$ Macs expressed pro-inflammatory surface receptors *CLEC5A* and *TREM1* and were enriched in pathways such as tumor necrosis factor alpha (TNFα) signaling, hypoxia, inflammatory response, glycolysis, and angiogenesis, mirroring pathways enriched in the IL-6 Q4 versus Q1 group in IMvigor210 (**Figure 3E**). In contrast, *CXCL9*$^+$ Macs expressed several genes related to antigen presentation and complement machinery, such as *C1QA/B/C*, and were enriched in interferon γ response and complement signaling.

As we found *SPP1*$^+$ Macs to be enriched in the TME of UC patients with high plasma IL-6, we next asked whether *SPP1*$^+$ Macs represent a major intratumoral source of IL-6. To address this, we performed RNAscope assessing for *IL-6* transcript on baseline UC tumors from the HCRN GU14-182 trial and subsequently stained the same tissue for CD68 by immunohistochemistry (IHC). Quantitative analysis with HALO confirmed that CD68$^+$ Macs expressed *IL-6* **(Figure S6A)**. On the same tumor sections, we also probed for *CXCL9* transcript by RNAscope, given the limitations of detecting secreted chemokines by traditional IHC. This analysis revealed that Macs were also a predominant source of *CXCL9*, and importantly, *IL-6* and *CXCL9* were produced by

distinct Mac populations within the same tumors, consistent with the *SPP1*$^{+}$ and *CXCL9*$^{+}$ Mac subsets identified by scRNA-seq **(Figure S6B-D)**. Interestingly, there was a significantly higher proportion of CD68^{+} Macs that expressed IL-6 in non-responders compared to responders (Mann-Whitney U test p = 0.008), suggesting that Macs are a major source of IL-6 within the TME, specifically in patients who progress despite ICB therapy **(Figure S6E)**. Additionally, we found that non-responders had a higher proportion of IL-6 producing cells that were CD68-expressing Macs (Mann-Whitney U test p = 0.02), suggesting that Mac-derived IL-6 may be pathologically important **(Figure S6F)**. Importantly, multiplex IHC (mIHC) performed on sequential slides to the RNAscope specimens showed that SPP1^{+}CD68^{+} Macs colocalized with *IL6* transcript signal, supporting that SPP1^{+} Macs are producers of IL-6 within the TME **(Figure 4F, Figure S7A).** Using mIHC and RNAscope, we also confirmed that HLA-DR^{+}CD68^{+} Macs co-localize with *CXCL9* transcript **(Figure 4G, Figure S7B-C)**, supporting the use of HLA-DR^{+}CD68^{+} Macs as a proxy for *CXCL9*$^{+}$ Macs **(Figure 4G, Figures 7B and C).**

We also utilized scRNA-seq data to identify *IL6* expression within the *SPP1*$^{+}$ Macs. For each patient, we averaged *IL6* expression across all cells and stratified patients into low (Q1) and high (Q4) *IL6* quartile groups based on the average expression values. We found *SPP1*$^{+}$ Macs to be a major source of *IL6* in the TME among patients with high *IL6* level (**Figure S7D**)**.** Notably, the frequency of *IL6*-expressing cells showed a significantly greater increase in *SPP1*$^{+}$ Macs compared to *CXCL9*$^{+}$ Macs from Q1 to Q4 (odds ratio: 15.59 vs. 6.03), consistent with the distinct functional roles of these Mac subsets (**Figure S7E**).

To further examine the spatial organization of *SPP1*$^{+}$ and *CXCL9*$^{+}$ Macs in the UC TME, we performed Visium 10X spatial transcriptomics analysis on tumors from 13 patients with UC from the HCRN GU14-182 trial. Clinical characteristics associated with these tumor samples are in **Table S3**. Leveraging the cell-type transcriptional profiles from our scRNA-seq cohort, we observed that *SPP1*$^{+}$ Macs and *CXCL9*$^{+}$ Macs occupied distinct niches within the TME (**Figure 4H**) and were negatively associated upon spatial co-localization analysis, especially in specimens

with high plasma CRP levels (**Figure 4I**). Consistent with hypoxia programs being upregulated in *SPP1*$^+$ Macs in our scRNA-seq cohort and UC TMEs linked to elevated plasma IL-6 in the IMvigor210 cohort, we also found that *SPP1*$^+$ Macs were positively associated with a hypoxia signature with regard to spatial co-localization analysis (**Figures 4H and I**). These findings suggest that microenvironmental pressures, such as hypoxia, may help drive the *SPP1*$^+$ Mac program in the UC TME. Furthermore, spatial co-localization analysis showed that *CXCL9*$^+$ Macs were preferentially positioned within regions enriched for a vasculature development signature(45) (**Figures S8A and B**). This may suggest that *CXCL9*$^+$ Macs occupy vascular-rich and immune-inflamed niches that facilitate T cell recruitment, whereas *SPP1*$^+$ Macs reside in hypoxic niches that are less permissive to T-cell activity.

A high CXCL9:SPP1 Mac ratio predicts improved OS across multiple ICB trials in UC

To better characterize the clinical relevance of the *SPP1*$^+$ and *CXCL9*$^+$ Mac populations in UC, we profiled the UC TME using scRNA-seq from available fresh tumor specimens derived from a subset of patients with MIBC enrolled on a trial of neoadjuvant pembrolizumab. We observed that the *CXCL9*$^+$ to *SPP1*$^+$ Mac ratio was lower in patients who did not achieve a clinical complete response to neoadjuvant pembrolizumab at the primary study endpoint (Mann–Whitney *U* test $p = 0.056$; **Figure 4J**). To further explore the implications of *SPP1*$^+$ and *CXCL9*$^+$ Macs in UC, we analyzed the correlation between the two gene ratio (*CXCL9*:*SPP1)* and OS using bulk RNA-seq data from 337 UC patients from the IMvigor210 trial, consisting of 187 distinct patients with primary lesions and 150 distinct patients with metastatic lesions(31). Higher *CXCL9*:*SPP1* ratios were associated with improved OS (**Figure 4K**).

The metastatic lesions from IMvigor210 spanned multiple anatomical sites including kidney, ureter, lymph node, lung, and more **(Figure S9A)**. When we assessed the 150 metastatic patients from IMvigor210 alone, we observed a consistent association, with lesions with higher *CXCL9:SPP1* ratios likewise correlating with patients' improved OS, indicating that the biology

captured by the *CXCL9:SPP1* ratio holds clinical significance in both primary and metastatic settings **(Figure S9B)**. Notably, comparison of the *CXCL9:SPP1* ratio distributions between IMvigor210 primary tumors and metastatic lesions revealed no significant difference **(**Mann-Whitney U test $p = 0.54$; **Figure 4L)**.

Beyond IMvigor210, we extended these findings to Caris Life Science's real-world data (RWD), analyzing bulk RNA-seq of metastatic lesions from a larger cohort of 422 UC patients prior to pembrolizumab treatment. The clinical characteristics of this cohort are described in **Table S4**. These samples spanned multiple metastatic sites, most prominently lymph node, lung, and liver **(Figure S9C)**. Consistent with IMvigor210, a higher *CXCL9:SPP1* ratio likewise significantly associated with improved OS in this independent Caris RWD metastatic cohort **(Figure 4M)**. We additionally examined patients' time on treatment (TOT) as a surrogate of progression-free survival for patients for which longitudinal treatment data was available (n=337). We observed that TOT was significantly associated with a higher *CXCL9:SPP1* ratio, suggesting that a higher ratio may be associated with more therapeutic durability of ICB **(Figure S9D)**. Notably, we examined the *CXCL9:SPP1* ratio predicted OS only in patients treated with ICB, but not in treatment-naïve TCGA UC cohorts of primary tumor **(Figure S9E)**.

Given that our deconvolution analysis of the IMvigor210 cohort also inferred enrichment of *NLRP3*$^+$ Macs in tumors linked to elevated plasma IL-6 (**Figure 4B**), we additionally investigated the prognostic value of the *CXCL9*$^+$ to *NLRP3*$^+$ Mac ratio by analyzing two-gene ratios comparing *CXCL9*$^+$ expression to various individual *NLRP3*$^+$ Mac markers (*IL1B, G0S2, CXCL2, EREG,* and *PLAUR)*. All five two-gene ratio scores correlated with OS in ICB-treated patients (**Figure S10A**); similar results were not observed in the TCGA cohort, which is comprised of clinically localized MIBCs treated with cystectomy (**Figure S10B**). This suggests that both the balance of *CXCL9*$^+$ versus *SPP1*$^+$ Macs and the balance of *CXCL9*$^+$ versus *NLRP3*$^+$ Macs in the UC TME are associated with clinical outcomes in the setting of ICB.

SPP1⁺ Macs are enriched in the UC TME versus normal-adjacent tissue.

As *SPP1⁺* Macs have been reported to underlie treatment resistance and poor outcomes in other cancers(17,40–42), we decided to characterize this Mac population in UC further. We found that among all Mac populations, only *SPP1⁺* Macs were significantly enriched in tumor versus normal tissues (Dirichlet-multinomial regression $p = 0.02$; **Figure 5A**). *SPP1* encodes osteopontin, which exists in intracellular and secreted isoforms and may be expressed by other cell types including cancer cells(46). To enable the isolation of *SPP1⁺* Macs and facilitate strategies to target them, we sought to define upregulated cell surface markers. Notably, the pattern recognition receptors *CLEC5A*(47) and *TREM1*(48) were highly expressed in *SPP1⁺* Macs (**Figure 4D**) and demonstrated increased expression in tumors from the IMvigor210 cohort linked to high versus low plasma IL-6 (**Figure 3D**). *CLEC5A* was exclusively upregulated by *SPP1⁺* Macs (**Figure S11A**), while *TREM1* was also expressed by *NLRP3⁺* and *FCN1⁺* Macs (**Figure S11B**). C-type lectin superfamily member 5 (CLEC5A) and triggering receptor expressed on myeloid cells 1 (TREM1) both associate with the DAP-12 adaptor protein, supporting their co-expression(49). We observed a significant positive correlation between *CLEC5A* and *TREM1* expression in TCGA UC cohort (**Figure S11C**).

We next isolated Macs co-expressing CLEC5A and TREM1 in fresh UC tissue samples (**Figure S11D**). Using this orthogonal approach, we discovered tumor tissue had a higher frequency of CLEC5A and TREM1 expressing Macs compared to normal-adjacent tissue (Wilcoxon signed-rank test $p < 0.05$; **Figures 5B and C**)**.** However, between normal-adjacent and tumor tissue, we did not observe differences in Mac frequency overall or within the CD45⁺ compartment (**Figure S11E**). These findings further suggest there may be TME-intrinsic cues driving the polarization of tumor-promoting *SPP1⁺* Macs.

IL-1β potentiates skewing of SPP1⁺ *Macs, whereas IFNγ drives* CXCL9⁺ *Macs*

To define cues in the TME that might impact the development of unfavorable *SPP1*$^+$ Macs, we bioinformatically inferred upstream ligands applying *SPP1*$^+$ Mac DEGs from scRNA-seq to the Ingenuity Pathway Analysis software and further evaluated these candidate ligands *in vitro* (**Figure S12A**). Macs were first differentiated from HD peripheral blood monocytes using M-CSF, skewed with exposure to each candidate, and their phenotype assessed by examining surface expression of CLEC5A and TREM1 (**Figures S12B-D**).

Among the inferred ligands, only IL-1β significantly increased individual and co-expression of CLEC5A and TREM1 **(Figures 5D-F and S12B-D)**. Notably, we also observed that *IL1B, IL1R2,* and *IL1RAP* demonstrated increased expression in tumors from the IMvigor210 cohort linked to high versus low plasma IL-6 (**Figure 3D**). We confirmed IL-1β upregulated several genes associated with *SPP1*$^+$ Macs, including *CLEC5A, TREM1, SPP1, IL1B*, and *IL6* using bulk RNA-seq and reverse-transcriptase quantitative polymerase chain reaction (RT-qPCR; **Figures 5G and H**). Interestingly, treatment with IL-1β also significantly decreased expression of *C1QC*, which is highly upregulated in *CXCL9*$^+$ Macs, supporting polarization away from a *CXCL9*$^+$ Mac phenotype (**Figures 4D and 5H**). We also confirmed IL-1β drove secretion of IL-6 and IL-1β (Wilcoxon signed-rank test $p < 0.01$ for both; **Figures 5I and S12E**). Since hypoxia pathways were enriched in *SPP1*$^+$ Macs from our scRNA-seq data, and HIF1α was identified as a predicted upstream activator of *SPP1*$^+$ Macs (**Figures 4E and S12A**), we sought to investigate the effects of hypoxia on IL-1β-skewed Macs. Under hypoxic conditions (1% O_2) compared to normoxia (21% O_2), IL-1β-skewed THP-1 monocyte-derived Macs exhibited increased TREM1 expression but no change in CLEC5A expression (**Figure S12F**).

Accordingly, we found evidence of IL-1β signaling in *SPP1*$^+$ Macs and *NLRP3*$^+$ Macs in scRNA-seq with these clusters demonstrating the highest percentage of *IL1R1* and *IL1RAP* expression amongst the different myeloid clusters (**Figure S12G**). We also found that plasma IL-1β levels were significantly higher in patients with UC as compared to age-matched HDs (**Figure S12H**). Analysis of our scRNA-seq dataset further revealed *IL1B* expression in *NLRP3*$^+$ Macs,

identifying these inflammasome-activated Macs as a notable source of IL-1β in the tumor microenvironment **(Figure S12I)**.

Interferon gamma (IFNγ) released by T cells, in the setting of adaptive anti-tumor immunity, has been associated with enhancement of antigen presentation, and IFNγ-related gene signatures have been correlated to favorable outcomes with ICB across multiple tumor types and analyses(50–52). Importantly, IFNγ-skewed Macs significantly decreased CLEC5A and TREM1 expression (Wilcoxon signed-rank test; $p < 0.001$; **Figure 5J**) and increased C-X-C motif chemokine ligand 9 (CXCL9) secretion (Wilcoxon signed-rank test $p < 0.01$; **Figure 5K**). We observed IFNγ signaling enriched in *CXCL9*$^+$ Macs (**Figure 4D**), and so we attempted to model *CXCL9*$^+$ Macs by skewing mono-derived Macs with IFNγ. Bulk RNA-seq revealed that these IFNγ-skewed Macs had an upregulation of *CXCL9*$^+$ Mac markers, including *CXCL9 and C1QC*, along with various genes associated with antigen presentation machinery (**Figure 5L**)**.** These findings support that IFNγ and IL-1β have opposing roles in driving immunostimulatory, antigen-presenting *CXCL9*$^+$ Macs versus pro-tumorigenic *SPP1*$^+$ Macs, respectively. These findings highlight how a balance of local cues in the TME can impact Mac transcriptional states.

Given the role of IL-1β in promoting the *SPP1*$^+$ Mac program, we sought to determine if this cellular state could be modulated pharmacologically. We found that treatment with an IL-1 receptor antagonist (IL1RA), an anti-inflammatory cytokine that competes with and blocks binding of active IL-1 to its receptor(53), before IL-1β polarization prevented skewing Macs to an *SPP1*$^+$ Mac program (**Figure 5M**). Interleukin 1 receptor-associated kinase 4 (IRAK4) is a serine/threonine kinase protein that relays intracellular signaling downstream of the IL-1 receptor(54). Treatment of monocyte-derived Macs with CA-4948, an IRAK4 inhibitor(55) before IL-1β polarization, decreased expression of genes associated with the *SPP1*$^+$ Mac program as well as decreased secretion of IL-6 (**Figures 5N and O**). Furthermore, CA-4948 treatment increased *C1QC* expression, suggesting this drug could skew tumor Macs towards a *CXCL9*$^+$ Mac phenotype (**Figure 5N**). These findings further establish the role of IL-1β signaling in driving

the *SPP1*$^+$ Mac transcriptional program and key cytokines involved in tumor-promoting inflammation in UC.

In vitro generated SPP1$^+$ *and CXCL9*$^+$ *Macs exhibit differential effects on T cell activity*

SPP1$^+$ Macs have been directly or indirectly associated with several genes encoding proteins that have been linked to tumor growth, progression, and treatment resistance(17,41–43,56). However, the mechanisms by which each of these factors may contribute to antitumor immunity are incompletely understood. To interrogate their immunosuppressive function, we co-cultured *in vitro* IL-1β-skewed mono-derived Macs (modeling *SPP1*$^+$ Macs) and our IFNγ-skewed mono-derived Macs (modeling *CXCL9*$^+$ Macs) with naïve CD8$^+$ T cells. CD8$^+$ T cells co-cultured with IL-1β-skewed Macs showed significantly reduced production of cytotoxic granules IFNγ, TNFα, and granzyme B compared to those co-cultured with IFNγ-skewed Macs (Wilcoxon signed-rank test $p < 0.0001$; **Figures 6A-D**). Additionally, we found that IL-1β-skewed Macs limited CD8$^+$ T cell proliferation compared to the IFNγ-skewed Macs (Wilcoxon signed-rank test $p < 0.01$, **Figures 6E and F**). However, reducing IL-1β skewing with CA-4948 treatment partially restored CD8$^+$ T cell effector function, enhancing IFNγ and TNFα production (Wilcoxon signed-rank test; $p < 0.01$; $p < 0.05$; **Figures 6G and H**). We found similar suppressive effects of our modeled *SPP1*$^+$ Macs on naïve CD4$^+$ T cells, limiting IFNγ and granzyme B effector granule production as compared to our modeled *CXCL9*$^+$ Macs (Wilcoxon signed-rank test $p < 0.05$; **Figures 6I-K**).

To further understand functional differences between these Mac states in an antigen-specific context, we modeled *SPP1*$^+$ and *CXCL9*$^+$ Macs by polarizing human THP-1-derived Macs with IL-1β or IFNγ, respectively, and co-culturing them with human NY-ESO-1-specific Jurkat CD8$^+$ T cells. Following pulsing with NY-ESO-1 peptide, IFNγ-skewed (*CXCL9*$^+$-like) Macs elicited markedly stronger T-cell activation than IL-1β-skewed (*SPP1*$^+$-like) Macs **(Figure S13A and B).** Consistent with this enhanced activation, *CXCL9*$^+$-like Macs expressed higher levels of HLA-A/B/C as compared to *SPP1*$^+$-like Macs and align with the enhanced antigen-presentation gene

programs observed in *CXCL9*$^+$ Macs in our scRNAseq of patient tumors **(Figures S13C and 4D).** This suggests that, in addition to their suppressive effects on naïve CD4$^+$ and CD8$^+$ T cells, *SPP1*$^+$ Macs are comparatively limited in their ability to activate antigen-specific T cells.

Distinct Patterns of T Cell Association for SPP1$^+$ *versus* CXCL9$^+$ *Macs*

Next, we examined spatial relationships between *SPP1*$^+$ and *CXCL9*$^+$ Macs and CD8$^+$ T cells. We revisited multiplex IHC from one responder and one non-responder in the HCRN GU14-182 trial, in which Mac subsets and CD8$^+$ T cells had been profiled on consecutive slides **(Figure S14A)**. To integrate these sections, we adapted MARQO(57), a recently developed open-source pipeline for user-guided whole-slide registration and overlay, enabling colocalization analyses between Mac subsets and CD8$^+$ T cells**.** Spatial graph-based analyses of cell centroids were used to quantify distances between CD8$^+$ T cells and either SPP1$^+$ or HLA-DR$^+$ Macs.

In the non-responder, SPP1$^+$CD68$^+$ Macs localized further away from CD8$^+$ T cells than HLA-DR$^+$CD68$^+$ Macs, with the distribution differing significantly by Kolmogorov-Smirnov test (p = 0.003) **(Figure S14B-D),** a pattern consistent across additional tissue islands from the same patient **(Figure S15)** as well as visually corroborated in higher magnification of the mIHC **(Figure S16A)**. Importantly, although the overall proportions of Mac subsets were relatively similar across the two patients **(Figure S16B)**, differences in CD8$^+$ T cell proximity to Mac subsets were statistically significant when comparing the responder versus non-responder (Responder vs. Non-responder: CD8$^+$:HLA-DR$^+$CD68$^+$, $p < 0.0001$; CD8$^+$:SPP1$^+$CD68$^+$, $p < 0.0001$). On average, the responder exhibited markedly closer distances between HLA-DR$^+$CD68$^+$ Macs and CD8$^+$ T cells compared to the non-responder, consistent with the possibility that these HLA-DR$^+$CD68$^+$ Macs (corresponding to *CXCL9*$^+$ Macs) may recruit CD8$^+$ T cells and contribute to response to ICB; whereas the non-responder exhibited further distances between SPP1$^+$CD68$^+$ Macs and CD8$^+$ T cells, suggesting *SPP1*$^+$ Macs may contribute to T cell exclusion in non-responders.

We also re-examined our Visium spatial transcriptomics data from UC tumors to investigate the spatial relationships between *SPP1*$^+$ and *CXCL9*$^+$ Macs and T cell subsets. We found that *SPP1*$^+$ Macs exhibited reduced co-localization with CD4$^+$ T and CD8$^+$ T cells, whereas *CXCL9*$^+$ Macs were more frequently found in proximity to T cells (**Figures 6L and S17**). This suggests that *SPP1*$^+$ Macs may contribute to an immunosuppressive TME by limiting T cell infiltration and function. In contrast, *CXCL9*$^+$ Macs may facilitate a more immunostimulatory niche that promotes T cell recruitment and activation. CXCL9 has been shown to be a potent chemoattractant for CXCR3$^+$ activated T cells and NK cells, thereby promoting their recruitment and enhanced local anti-tumor immune activity(15–17).

IL-6 limits CD8$^+$ and CD4$^+$ T cell effector cell differentiation.

To directly test whether IL-6 mediates the suppressive activity of *SPP1*$^+$ Macs, we performed co-culture experiments of naïve CD8$^+$ T cells with in vitro–modeled *SPP1*$^+$ Macs in the presence of the IL-6 receptor–blocking antibody tocilizumab. Blockade of IL-6 signaling partially restored T cell effector function, with tocilizumab-treated CD8$^+$ T cells exhibiting significantly increased IFNγ and TNFα production relative to isotype control-treated CD8$^+$ T cells in co-culture with *SPP1*$^+$ Macs **(**Wilcoxon signed-rank test $p < 0.05$; **Figures 7A and B).** Although tocilizumab attenuated *SPP1*$^+$ Mac-mediated suppression, it did not normalize CD8$^+$ T cell function to that of T cells alone, suggesting that additional Mac-derived factors likely cooperate with IL-6 in mediating this effect **(Figure S18A)**. These findings provide direct functional evidence that IL-6 is required for *SPP1*$^+$ Mac–mediated suppression of CD8$^+$ T cells.

Building on this observation, we next investigated whether IL-6 alone was sufficient to impair adaptive immune cell function. IL-6 was recently proposed to suppress ICB response through limiting effector CD8$^+$ T cell differentiation(33). To expand upon this, we cultured HD naïve CD8$^+$ T cells with IL-6 over five days and found significantly decreased effector granule

production, consistent with impaired differentiation to an effector T cell phenotype (Wilcoxon signed-rank test $p < 0.01$; **Figures 7C and D**). Similar suppressive effects of IL-6 were observed for $CD4^+$ T cells phenotype (Wilcoxon signed-rank test $p < 0.05$; **Figures 7E and F**).

To understand the mechanisms underlying IL-6 suppression of T cell function, we performed bulk RNA-seq of naïve $CD8^+$ and $CD4^+$ T cells with IL-6. IL-6 induced several genes in $CD8^+$ T cells, of which the most highly upregulated was *SOCS3,* which is known as a negative regulator of IL-6 signaling and has also been reported to induce an "immune paralysis" state in T cells that is less responsive to stimulation(58,59) (**Figure 7G**). When IL-6 was added to $CD8^+$ T cells activated with anti- cluster of differentiation 3 (CD3) and cluster of differentiation 28 (CD28), *SOCS3* remained the only significant DEG (**Figure 7H**). We similarly found that IL-6 increased *SOCS3* expression in both naïve and activated $CD4^+$ T cells (**Figures 7I and J**). Importantly, similar suppressive effects on $CD4^+$ and $CD8^+$ T cells were not observed in the presence of recombinant IL-1β or SPP1 protein and were specific to the naïve T cell compartment (**Figures S18B-E).** Therefore, IL-6 produced by *SPP1*$^+$ Macs in the UC TME, potentially along with other cells, may directly suppress anti-tumor T cell cytotoxicity through upregulation of suppressor of cytokine signaling 3 (SOCS3).

Interestingly, prior investigation has shown that CRP can directly impair T cell function(60), and consistent with this, we found recombinant CRP reduced IFNγ production by $CD8^+$ T cells in vitro **(Figure S18F)**. While we cannot rule out that CRP may also exert additional direct effects on T cell function, the extent to which CRP may be produced locally within the TME and also contribute to suppression of anti-tumor immunity has not been adequately explored and warrants further investigation.

To confirm the relationship between plasma IL-6 and T cell transcriptional programs in patients with UC, we performed scRNA-seq on peripheral blood mononuclear cells (PBMCs) from nine patients with UC, grouping them into high, medium, and low IL-6 groups based on their plasma IL-6 levels (**Figure S18G**). We identified naïve $CD8^+$ and $CD4^+$ T cell clusters based on

upregulation of *CCR7*, *IL7R,* and *SELL* (**Figures S18H and I**). We found markers of IL-6 intrinsic signaling, namely upregulation of *SOCS3*, *STAT3*, and *JAK3*, most highly expressed by $CD4^+$ and $CD8^+$ T cells from patients with UC in the highest IL-6 group (**Figures 7K and L**). Furthermore, these patients had T cells with the lowest levels of cytotoxic markers, *PRF1, GZMB, TNF, and IFNG,* and the stem-like progenitor marker *TCF7*/Tcf1, while patients with lower IL-6 plasma levels had higher expression of these functional markers (**Figures 7K and L**). These findings provided further support that IL-6 suppresses naïve $CD8^+$ and $CD4^+$ T cells in UC.

To determine if the plasma of patients with UC could impact T cell expression of SOCS3, we added plasma from either HDs or patients with UC (containing higher levels of IL-6; **Figure S18J**) to T cells from another HD. After 24-hour culture, plasma from patients with UC induced significantly more SOCS3 in $CD8^+$ and $CD4^+$ T cells than HD plasma (Mann-Whitney *U* test; $p < 0.01$; $p < 0.001$; **Figures 7M and N; Figures S18K and L**). We observed a significant and strong positive correlation between plasma IL-6 levels and the frequency of $SOCS3^+$ $CD8^+$ T cells (Pearson's $r = 0.91$; $p < 0.0001$; **Figure 7O**) and $SOCS3^+$ $CD4^+$ T cells (Pearson's $r = 0.84$; $p < 0.0001$; **Figure 7P**), supporting that IL-6 within the plasma was driving SOCS3 expression. Therefore, IL-6 may limit $CD8^+$ and $CD4^+$ cytotoxic T cell differentiation in patients with UC through SOCS3 induction.

Discussion:

Diverse peripheral blood markers, including CRP, have been associated with poor outcomes and ICB resistance across a wide range of studies and tumor types(13,14,23). However, the cellular and molecular mechanisms linking elevated plasma CRP to the tumor TME remain poorly understood. We demonstrated that plasma CRP is associated with poor outcomes across multiple ICB-treated cohorts of patients with UC, on-treatment decline in CRP is associated with improved clinical outcomes in a mechanism of action-dependent manner, plasma CRP and IL-6 are highly correlated consistent with the known role of IL-6 in stimulating CRP

production from hepatocytes, and UC TMEs linked to elevated plasma CRP, IL-6, and CSF-1 are enriched in genes related to IL1 signaling, *SPP1*$^+$ Macs, and basal-squamous bladder cancer cells.

Through examining myeloid cells in the UC TME at high resolution and creating the largest UC scRNA-seq atlas to date, we further demonstrated a dichotomy of Macs in the UC TME with *SPP1*$^+$ Macs associated with unfavorable ICB response and *CXCL9*$^+$ Macs associated with favorable ICB response. Across multiple ICB-treated cohorts in UC, a higher *CXCL9:SPP1* ratio in both primary tumors and metastatic lesions was associated with improved clinical response, indicating that this Mac axis reflects fundamental tumor biology with clinical relevance in both localized and advanced disease. This Mac dichotomy does not recapitulate M1 versus M2 polarization and is consistent with observations made in other tumor types.

We identified IL-1β signaling as a major driver of the *SPP1*$^+$ Mac transcriptional program, while IFNγ signaling drives the expression of the *CXCL9*$^+$ Mac program. Furthermore, we identify CLEC5A and TREM1 as two novel surface markers differentially expressed by *SPP1*$^+$ Macs. Key cytokines expressed by *SPP1*$^+$ Macs linked to tumor-promoting inflammation, specifically IL-6, are associated with resistance to ICB in UC and were shown to impair effector CD8$^+$ and CD4$^+$ T cell differentiation through *in vitro* Mac-T cell co-cultures. To corroborate these findings, we directly visualized *IL6* and *CXCL9* expression in baseline UC tumors using RNAscope combined with IHC, confirming that distinct Mac subsets are a prominent source of these cytokines in situ. Multiplex IHC together with MARQO-based spatial analysis and Visium spatial transcriptomics further demonstrated that these Mac subsets are spatially distinct. Consistent with CXCL9's known role in promoting T cell recruitment, *CXCL9*$^+$ Macs localized in closer proximity to CD8 T cells in responders, whereas *SPP1*$^+$ Macs were spatially segregated from T cells in non-responders, providing direct tissue-level validation of the functional dichotomy of these subsets. Our comprehensive analysis of Macs in human UC reveals a dynamic interplay of immune pathways in the UC TME, linking tumor-promoting inflammation to ICB response.

Our study uncovers tumor-promoting inflammatory positive feedback loops within the TME that may be amenable to therapeutic modulation. We found that IL-1β skews Macs away from an antigen-presenting phenotype to a tumor-promoting *SPP1*$^{+}$ Mac state that secretes IL-6, which then reduces T cell production of IFNγ; this reduction in IFNγ signaling also contributes to the shift in Macs towards an *SPP1*$^{+}$ Mac phenotype, perpetuating this cycle. Our findings also suggest another positive feedback loop in which IFNγ produced by tumor-infiltrating T cells promotes the differentiation or activation of *CXCL9*$^{+}$ Macs, which in turn recruit additional CXCR3^{+} T cells that further amplify local IFNγ production. Our insights into the UC TME stem from data from ICB-evaluating clinical trials and human specimens supported by experimental results. However, our systems were limited in assessing the influence of other intertwined or redundant cell types and pathways on this biology and its impact on ICB response. Notably, Bill *et al*. demonstrated that transcriptional programs associated with *CXCL9:SPP1* Mac polarity were expressed in a coordinated manner across diverse cell types in individual TMEs in squamous cell cancer of the head and neck(17). Further investigation will allow us to elucidate the roles of additional cells and cytokines that may affect anti-tumor immunity, and the origin of monocytes that develop into the *SPP1*$^{+}$ Mac phenotype, enabling us to most optimally re-program the TME. Nonetheless, our study disentangles several intricacies of the UC TME, unveiling clear pathways harboring promising therapeutic targets.

Our results expand on the mechanistic basis by which IL-6, associated with *SPP1*$^{+}$ Macs, may impact ICB response. We show that blockade of IL-6 signaling with the IL-6R antibody tocilizumab partially restored CD8^{+} T cell effector function in co-culture with *SPP1*$^{+}$ Macs, significantly enhancing IFNγ and TNFα production. This provides direct evidence that IL-6 is required for *SPP1*$^{+}$ Mac–mediated T cell suppression and highlights the therapeutic potential of targeting IL-6 in this context. Our evidence of IL-6 impairment of T cells through upregulation of *SOCS3* further reinforces the causal relationship between increased plasma IL-6 and poor outcomes in UC, as well as pre-clinical work showing IL-6/IL-6 receptor (IL-6R) abrogation

565 combined with anti-PD-1, improves tumor control(33). Interestingly, circulating myeloid cells have
566 also been shown to induce “T cell paralysis” in patients with biliary tract cancer through
567 upregulation of SOCS3 in T cells(59), and IL-6 signaling through SOCS3 limits T cell immunity in
568 a murine model of colon cancer(61). Further studies are required to define how *SOCS3*
569 mechanistically enforces T cell dysfunction downstream of IL-6.

570 *SPP1*$^{+}$ Macs emerge from our data as a key intratumoral source of IL6, but these findings
571 do not exclude substantial IL-6 production by other stromal populations such as fibroblasts.
572 Indeed, prior work has shown that *CXCL9*$^{+}$*–SPP1*$^{+}$ Mac polarity aligns with transcriptional
573 programs shared across cell types in the TME, including Macs and fibroblasts(17). These
574 inflammatory circuits appear to be coordinately regulated across multiple cell types within
575 individual TMEs and the crosstalk between Macs and fibroblasts that reinforces tumor-promoting
576 inflammation in UC warrants further investigation.

577 The identification of *SPP1*$^{+}$ Macs as a distinct immunoregulatory cell associated with ICB
578 resistance carries important clinical implications, and our mechanistic insights highlight several
579 potential translational opportunities. Our data indicate that the *SPP1*$^{+}$ Mac program is targetable
580 through multiple modalities, including blockade of upstream drivers, direction inhibition of *SPP1*$^{+}$
581 Mac themselves, and suppression of downstream mediators. In terms of upstream regulation, we
582 show that IL-1β in the tumor milieu promotes the skewing of *SPP1*$^{+}$ Macs and their production of
583 IL-6, suggesting that therapeutics directed at the IL-1 signaling axis could potentially modulate
584 this pathogenic axis. Though targeting IL-1β itself has been similarly unsuccessful in the
585 clinic(62,63), targeting alternative nodes along the IL-1 signaling axis, such as IRAK4, may offer
586 advantages. Indeed, a phase I trial combining IRAK4 inhibitor (CA-4948) plus pembrolizumab in
587 patients with mUC progressing despite prior ICB, seeking to reprogram *SPP1*$^{+}$ Macs and
588 overcome resistance, has been initiated to test this concept (ClinicalTrials.gov identifier:
589 NCT06439836). Notably, we also identify CLEC5A and TREM1 as selectively enriched surface
590 receptors on *SPP1*$^{+}$ Macs in UC, raising the possibility of subset-restricted therapeutic depletion

using antagonistic antibodies. Approaches to target IL-6 signaling to improve ICB outcomes in mUC in the clinic have not yet been successful(64), even though anti-IL-6R monoclonal antibodies are used widely in the clinic for cancer patients with tocilizumab used to dampen cytokine release syndrome as a side effect of chimeric antigen receptor therapy. This may be due to the lack of enrichment of patients who might derive the most benefits from this strategy and/or the redundancy of mechanisms related to *SPP1*$^{+}$ Mac-associated impairment of anti-tumor immunity highlighting the potential need to "reprogram" Macs towards the *CXCL9*$^{+}$ program to translate into better patient benefit. However, there are active trials evaluating the combination of IL-6R blockade and ICB that across solid tumor types that will provide more insight as to whether targeting IL-6 signaling will provide additional therapeutic benefit to ICB including assessing tocilizumab and atezolizumab in non-small cell lung carcinoma (NCT04691817), as well as investigating sarilumab with anti-CTLA4 ipilimumab, anti-PD-1 nivolumab, and anti-LAG3 relatlimab (NCT05428007). Neoadjuvant combination of atezolizumab, tocilizumab, and anti-A2AR/A2BR etrumadenant is also being tested in prostate cancer (NCT03821246).

Finally, our analyses of circulating CRP and IL-6 reveal associations with *SPP1*$^{+}$ Mac linked inflammatory states, suggesting that these readily measurable plasma markers could be integrated with already existing biomarkers (e.g., PD-L1 status, tumor mutational burden, and genomic alterations such as DNA damage repair mutations) to help stratify patients most likely to benefit from therapies targeting this *SPP1*$^{+}$ Mac axis. Such peripheral biomarkers could guide the selection of individuals with IL-6/CRP-high disease who may be enriched for *SPP1*$^{+}$ Mac-driven immunosuppression and therefore more responsive to therapeutic interventions.

Our study provides novel insights into the tumor immune landscape of UC, linking elevated plasma IL-6 and CRP to tumor-promoting inflammation and Mac-driven immune regulation in the UC TME. Specifically, we identify a functional dichotomy of *SPP1*$^{+}$ and *CXCL9*$^{+}$ Mac subsets, which shape anti-tumor T cell responses and are associated with unfavorable and favorable ICB outcomes, respectively. Further research is needed to determine whether targeting these Mac

subsets can enhance cytotoxic T cell responses and overcome ICB resistance in UC and other cancers.

Acknowledgements:

We are grateful for the patients who volunteered to participate in these studies, the Mount Sinai Genitourinary Medical Oncology and Urology providers who screened, enrolled, and cared for these patients, the Mount Sinai Biorepository and Pathology Core who aided with tissue accrual, the Mount Sinai Genomics Core for the scRNA-seq and Visium CytAssist, and the Mount Sinai Human Immune Monitoring Core (HIMC) for assistance with the CRP, O-Link and Visium spatial transcriptomics assays. Thank you to Sanjana Shroff, Disha Chowhan, and Robert Sebra for help with scRNA-seq library preparation. Thank you to Apex for Youth for funding Karen Lee's summer research experience. Thank you to Bridget Keenan and Lawrence Fong at UCSF for their advice on co-culturing T cells with patient plasma. We are grateful to all members of the Bhardwaj Lab for their support and scientific discussions. We are grateful for Christopher McClain for his assistance in helping prepare the NY-ESO-1 specific Jurkat cells. This publication is based on research using data from data contributors Roche that has been made available through Vivli, Inc. Vivli has not contributed to or approved, and is not in any way responsible for, the contents of this publication. The funders had no role in study design, data collection and analysis, decision to publish, or manuscript preparation. MT was supported by a National Institutes of Health (NIH) grant: 5F30CA275269. SI was supported by an NIH 5T32CA078207 grant. SI and MDG were supported by a Merck Oncology Translational Studies Program Award. SG was partially supported by NIH grants: U24 CA224319 and U01 DK124165. SG, NB, and MDG were partially supported by P30 CA196521. This work was also supported by the NIH 5R01CA249175.

Author Contributions:

MAT conceptualized and performed experiments, analyzed the data, interpreted the results, and wrote and revised the manuscript. BAC and SY performed analyses, interpreted the results, and wrote and revised the manuscript. SI conceptualized and performed experiments, analyzed the data, interpreted the results, and revised the manuscript. DY and AMF assisted with experiments, data analysis, and data interpretation. JA assisted with conceptualizing, performing, and analyzing experiments. KL and AA assisted with experiments. EGK, IDS, RB, SG, AC, LW, MB, and SG assisted with data analysis. KB, ZL, MGB, RB, CCC, and SKS contributed to sequencing and spatial profiling experiments. KY, SM, JPS, and AH provided experimental advice. RM and JPS are urologic surgeons who collected clinical specimens from patients for this study. DC, MDG, and NB provided research oversight by helping conceptualize experiments, interpret data, and write and revise the manuscript.

Inclusion and Diversity:

We aimed to achieve ethnic and other types of diversity in the recruitment of human subjects for this manuscript. While citing references scientifically relevant for this work, we also attempted to promote gender balance in our citations.

Methods:

Clinical trial sample collection for CRP analysis

To examine the relationship between plasma CRP levels and ICB outcomes in patients with UC, we analyzed six clinical trial cohorts, using patients with available CRP data. Three phase 3 clinical trial cohorts (IMvigor130 (*n* = 691), IMvigor211 (*n* = 862)) and three phase 2 clinical trial cohorts (IMvigor210 (*n* = 406), GU14-182 (*n* = 108)) were collected for this study. Study data packages including CRP and outcomes data were provided by Hoffmann-La Roche through Vivli Center for Global Clinical Research Data (Research project 10046) for bladder cancer clinical trials: IMvigor211, (ClinicalTrials.gov identifier: NCT02302807), IMvigor130 (ClinicalTrials.gov

identifier: NCT02807636), IMvigor210 cohort 1 (ClinicalTrials.gov identifier: NCT02951767), IMvigor210 cohort 2 (ClinicalTrials.gov identifier: NCT02108652). For HCRN GU14-182 trial (ClinicalTrials.gov identifier: NCT02500121), high sensitivity CRP (hs-CRP) was measured in plasma using ELISA (Catalog #DCRP00; R&D Systems Inc., Minneapolis, MN, USA), following the manufacturer's instructions. The OS was calculated from the randomization day (phase 3) or treatment start day (phase 2) to death from any cause, with patients alive at the time of review censored at their last contact.

Baseline CRP and CRP dynamic analysis

To examine the relationship between pre-treatment plasma CRP levels and poor outcomes, patients with baseline CRP data were categorized into four quartile groups in each clinical trial: the Q1 group consists of patients with the lowest CRP levels, while the Q4 group includes those with the highest CRP levels. To investigate the association between decline in post-treatment plasma CRP with improved outcomes, CRP ratio was calculated as the post-treatment CRP value divided by the pre-treatment CRP value. For the post-treatment CRP values, we used the next available time point in the treatment cycle following the baseline measurement. For IMvigor130 and IMvigor210, Cycle3 Day1 values were used and for IMvigor211, Cycle4 Day1 values were used. For the CRP dynamics analysis, patients were stratified into two groups using the median value. Both quartile groups and median groups were determined from all samples, ICB arm and control arm.

Olink, Target 96 Panel

To interrogate cytokines in the plasma of patients with UC from the HCRN GU14-182 study and from the other patients, we utilized the O-link proteomics Inflammation panel (ThermoFisher). This panel encompassed 92 paired oligonucleotide antibody-labeled probes targeting proteins related to several immune-oncology pathways. In a 96-well plate, 1 μL of patient plasma was mixed with

3 μL of an O-Link incubation mix and incubated overnight at 4°C. The following day, O-link extension reagent mix containing PCR polymerase was added and placed into a thermal cycler a 1.5-hour pre-amplification step. In the detection phase, 2.8 μL from each well was mixed with 7.2 μL of a detection mix and placed on a 96-96 Dynamic Array Integrated Fluidic Circuit along with the 92 oligonucleotide pairs. The chip was assessed with the Fluidigm BioMark qPCR reader. Samples were run individually with blanks and inter-plate batch controls. Additional details pertaining to assay protocols and validations can be obtained from the O-link supplier (https://www.olink.com). Quality control and normalization were performed as per manufacturer's protocols. Log_2 fold-change relative to the mean protein expression of healthy plasma controls (n = 10 pooled healthy donors) was calculated and expressed as Normalized Protein eXpression (NPX). NPX values were used for heatmap and bar-plot analyses. Due to the log_2 scale, an increase of 1 NPX corresponds to a doubling of protein concentration. NPX values were used for relative quantification only and were compared across two independently conducted projects using reference bridging samples to ensure consistency.

IL-1β cytokine analysis in plasma

Plasma IL-1β levels were determined using Human IL-1β/IL-1F2 QuicKit ELISA (R&D Systems, cat. # QK201) and following manufacturer protocols. Wilcoxon signed-rank tests were used to compare plasma cytokine NPX levels across disease stage (* p<0.05; ** p<0.01; *** p<0.001; **** p<0.0001).

IMvigor210 RNA-seq sample collection

Bulk RNA-seq data from the IMvigor210 cohort was obtained via the IMvigor210CoreBiologies R package (http://research-pub.gene.com/IMvigor210CoreBiologies/). Raw count data were used for DEG analysis, while normalized fragments per kilobase of transcript per million mapped reads values were calculated for gene ratio analysis.

TCGA sample collection

Expression and survival data for TCGA bladder cancer (n = 428)(32) were obtained from UCSC Xena (http://xena.ucsc.edu) (GDC TCGA Bladder Cancer)(65). Transcripts per million (TPM) values, processed using TCGA's standard pipeline (https://docs.gdc.cancer.gov/Data/Bioinformatics_Pipelines/Expression_mRNA_Pipeline/), were used for analysis.

Differentially expressed gene analysis

To characterize DEGs, DESeq2 R package (v 1.46.0) was used(66). The samples with available IL-6 measurements were divided into four groups based on the quartile values of each measurement in each cohort. DEGs were identified by comparing the highest quartile group (Q4) against the lowest quartile group (Q1). The genes with false discovery rate (FDR)-adjusted *p*-value < 0.05 and $|Log_2$fold-change (FC)| > 0.58 were defined as DEGs. Volcano plots were created to visually represent the most biologically significant genes by plotting statistical significance against Log_2FC. Two vertical dashed lines indicate fold change cutoffs at −0.58 and 0.58, defining one of the thresholds for DEGs. A horizontal dashed line represents an FDR-adjusted *p*-value of 0.05, marking another threshold for DEG identification.

Gene set overrepresentation analysis

To identify clinically relevant biological pathways associated with plasma CRP levels, overrepresentation analysis was performed using DEGs. The analysis was conducted with the msigdbr R package (v7.5.1), utilizing hallmark gene sets(44).

RNAscope assay and HALO analysis

Automated RNAscope™ in situ hybridization (ISH) assay detects high target signals with low background in human tissues. The experiment was conducted at the Neuropathology Brain Bank and Research CoRE at the Icahn School of Medicine at Mount Sinai. The assay was performed using the Leica BOND RX (LS) automated platform. Serial formalin-fixed paraffin-embedded (FFPE) sections (4 um) of GU14-182 human primary baseline UC cases were freshly sectioned at the Icahn School of Medicine at Mount Sinai Biorepository and Pathology CoRE and stained with the automated RNAscope™ 2.5 LS Duplex Reagent Kit (ACD Bio-Techne, cat. # 322430) using RNAscope™ 2.5 LS Probe Hs-IL6-C1 (ACD Bio-Techne, cat. # 310378-C1). Human *IL6* probes (ACD Bio-Techne, cat. # 310378) and human *CXCL9* probes (ACD Bio-Techne, cat. # 440168-C2) were used. The signal was detected using the Bond Green Chromogen kit (Leica Biosystem, cat. # DC9913). HALO Image Analysis Platform version 4.0.5107 and HALO AI version 4.0.5107 (Indica Labs, Inc) were used to perform whole slide quantification of *IL6* ISH probe. For this, ISH4.2.11 algorithm was used to analyze the *IL6* chromogenic probe on a cell-by-cell basis, measuring copy number per cell, directly calculating the H-score, performing deconvolution, object phenotyper and cell mark-up.

Fast gene set enrichment analysis

To assess which cell types were prevalent in patients with an elevated IL-6 level from bulk RNA-seq data of IMvigor210, fast gene set enrichment analysis (FGSEA) was performed (bioRxiv 10.1101.060012). The FGSEA method calculated the normalized enrichment score (NES) to quantitatively assess how each cell type marker is overrepresented at the top or bottom of pre-ranked list of genes (highly expressed genes in tumor with an elevated IL-6 or vice versa). DEGs from bulk RNA-seq data of IMvigor210 were analyzed based on the cell types from the scRNA-seq data. If none of the marker genes for a given cell type met the threshold ($|Log_2FC| > 1$, adj. p-value < 0.05, and pct.1 ≥ 0.5), that cell type was excluded from the analysis (e.g., T.CD4.cytotoxic). Softwares and packages used in this study are listed in **Table S5**.

CXCL9:SPP1 and macrophage marker gene ratio analysis

The *CXCL9:SPP1* ratio has been suggested as a surrogate marker for Mac polarization within TME(17). To highlight the clinical significance of macrophage states in UC, we assessed the relationship between the *CXCL9:SPP1* gene ratio and OS using bulk RNA-seq data. Given *NLRP3*$^{+}$ Macs are also enriched in BC TME, we also explored the relationship between the two gene ratios of *CXCL9:NLRP3* Mac marker genes. The marker genes of *NLRP3*$^{+}$ Macs cluster were identified using FindAllMarker function in Seurat R package (v 4.3.0)(67). The top 5 marker genes of *NLRP3*$^{+}$ Macs are *EREG*, *IL1B*, *PLAUR*, *SAMSN1*, and *G0S2*.

Human study oversight

The collection of human tissue samples for this study was approved by the Mount Sinai Institutional Review Board (IRB) under the Tisch Cancer Institute at the Icahn School of Mount Sinai's (ISMMS) Genitourinary Cancer Biorepository (IRB#: 10-1180). Patient samples from the HCRN GU-14-182 trial were also collected under ISMMS IRB# 20-4018. Every patient provided written informed consent before enrolling in this study.

Dissociation of bladder tissue to single-cell suspensions

UC tumor and normal adjacent tissue specimens were obtained from the operating room and grossed by surgical pathology. Immediately, tumors were immersed in RPMI 1640 media and added to ice for transport to the laboratory. Upon receipt, tumors were minced using a razor blade and subjected to simultaneous enzymatic and mechanical digestion using the Miltenyi Biotec Human Tumor Dissociation Kit (Miltenyi Biotec, cat. # 130-095-929) and gentleMACS (Miltenyi Biotec, cat. #130-096-427), set to the 37C_h_TDK_2 program. Resultant cells were sequentially filtered through 100 µm, 70 µm, and 40 µm strainers to remove debris. Single cell suspensions were counted for viability using Trypan blue (Corning, cat. # 25-900-CI) and Countess II

Automated Cell Counter (ThermoFisher) and immediately stained for flow cytometry analysis or scRNA-seq.

Isolation of PBMC and plasma from patients with UC and HDs.

Fresh whole blood samples were obtained from patients with UC before the start of surgery. Peripheral blood was collected into 10-mL EDTA tubes and transported. Once received, whole blood was spun at 1000g for 10 minutes, and plasma was removed and frozen down. PBMCs were isolated by centrifugation over Ficoll400 cell separation solution (density 1.077 g/mL; GE Healthcare, cat. # 17-1440-03). Red blood cells were removed by treatment with ACK lysis buffer (Gibco, cat. # A10492-01), and then PBMCs were counted for viability using Trypan blue. Healthy donor buffy coats and plasma were obtained from the New York Blood Bank and processed in the same way.

scRNA-seq

Droplet-based scRNA-seq was conducted using the 10X Genomics Chromium Single Cell 3' and 5' GEX V3 platforms, following manufacturer protocols. UC tumor cells, normal-adjacent cells, and PBMCs were suspended in phosphate buffered solution (PBS, Gibco, cat. #14190144) with 0.04% bovine serum albumin (BSA, Fisher Bioreagents, cat. # 9048-46-8) prior to loading onto the 10X platform. Only specimens exhibiting $\geq$80% viability were loaded. Libraries were prepared and then sequenced on an Illumina NovaSeq S4 flow cell (Illumina, CA, USA). Matched specimens from the same patient were processed in parallel during library preparation and sequenced on the same flow cell to reduce batch effects between samples. Details on previously deposited data are listed in **Table S5.**

Raw data processing, quality control, and Seurat analysis of scRNA-seq

Raw scRNA-seq data was aligned and quantified by the Cell Ranger Single-Cell Software Suite (version 3.0, 10x Genomics) and with the GRCh38 human reference genome. This created a raw unique molecular identifier (UMI) count matrix. This was then created into a Seurat object using the R package, Seurat. Cells expressing over 15% or more of mitochondrial genes, representing dead or dying cells, were deleted for quality control. Cells with unique feature counts over 2,500 or less than 200 were also deleted to remove potential doublets or empty droplets, respectively. Additional potential doublets that escaped through this filter step were predicted and deleted by applying the DoubletFinder R package (v.2.0.4) to each specimen(68). To combine specimens for analysis, the top 2,000 variable genes were applied to create anchors using the Seurat's FindIntegrationAnchors function. Next, Seurat's IntegrateData function was performed, which created a new matrix consisting of 2,000 features. Elbow plots were generated to determine the number of principle components for clustering. Cells were visualized using Uniform Manifold Approximation and Projection (UMAP) for dimensionality reduction. We annotated cell types by adopting our previous work(39) using Seurat's FindTransferAnchors and TransferData functions. Seurat's FindAllMarkers function was applied to identify marker genes of each cell type. Log2|FC| ≥ 1, adj.p.val < 0.05, and pct.1 ≥ 0.5 were used as cut-offs for cell type markers. To identify DEGs between two cell types, $Log_2FC \geq |0.58|$ and adj.p.val < 0.05 were used as cut-offs. We applied a Dirichlet multinomial regression to compare the abundance of Mac populations between tumor and normal tissues, which considers the compositional nature of the data, as done in a previous study(69). Software and packages used in this study are listed in **Table S5**.

RNAscope and immunohistochemistry on formalin-fixed and paraffin-embedded bladder tumors

Single RNAscope red in situ hybridization was performed using the Leica Bond RX system to stain two consecutive tissue sections from ten GU14-182 formalin-fixed, paraffin-embedded tumor samples (4 µm thick) for *CXCL9* (Hs-*CXCL9*-C2, cat. # 440168-C2, Advanced Cell Diagnostics, Inc.) or *IL6* (Hs-*IL6*-C1, cat. # 310378-C1). The signal was detected using the

RNAscope kit (cat. # 332150) and Bond Polymer Refine Red Detection (cat #. DS9390) on the Leica Bond RX platform, following the manufacturer's protocol. Subsequently, CD68 immunohistochemistry was performed on the same sections using the Ventana Discovery Ultra autostainer (Roche). The sections were incubated with CD68 primary antibody (clone KP1, Roche, cat. # 05278252001), followed by OmniMAP HRP anti-mouse secondary antibody (Roche, cat. # 760-4310). Signal detection was achieved using the Discovery Yellow HRP kit (Roche, cat. # 760-250). Hematoxylin and bluing reagents (Roche, cat. # 760-2021 and cat. # 760-2037) were applied for counterstaining. RNAscope in situ hybridization combined with immunohistochemistry was conducted at the Neuropathology Brain Bank & Research CoRE, Icahn School of Medicine at Mount Sinai. Whole tissue sections on the slide were captured as high-resolution digital images using a NanoZoomer S210 digital slide scanner (Hamamatsu). Cell phenotyping, deconvolution, markup, and cell counting were performed using the HALO Image Analysis Platform and ImageJ software with the Cell Counter plugin (Fiji ImageJ 1.54p, National Institutes of Health). Whole slide scanning and HALO image analysis were performed at the Biorepository and Pathology CoRE at the Icahn School of Medicine at Mount Sinai.

Multi-chromogen immunohistochemistry on formalin-fixed and paraffin-embedded bladder tumors

Staining was conducted on consecutive tissue sections from tumor samples of GU14-182 patients. Formalin-fixed, paraffin-embedded sections (4 µm thick) were used for multi-chromogen sequential immunohistochemistry. Staining was performed using the Ventana Discovery Ultra system (Roche Diagnostics) with RUO Discovery Universal reagents. Primary antibodies were divided into two panels targeting CD68 (clone KP-1, Roche, cat. #. 790-2931), SPP1 (Millipore Sigma, cat. # HPA027541,), HLA-DR (clone TAL.1B5, Agilent, cat. # M0746), CD8 (clone SP57, Roche, cat. # 790-4460), and Pan-Cytokeratin (clone AE1/AE3, Abcam, cat. # ab27988). Signal detection was performed using OmniMap Purple for HLA-DR or CD8, Teal for CD68, and DAB

for Pan-Cytokeratin or SPP1. Hematoxylin was used for nuclear counterstaining. Whole tissue sections were digitized as high-resolution images using a NanoZoomer S210 digital slide scanner (Hamamatsu). Cell phenotyping, deconvolution, markup, and cell counting were conducted using the HALO Image Analysis Platform and ImageJ software with the Cell Counter plugin (Fiji ImageJ 1.54p, National Institutes of Health). Immunohistochemistry, whole slide scanning and HALO image analysis were performed at the Biorepository and Pathology CoRE at the Icahn School of Medicine at Mount Sinai.

Visium CytAssist Spatial Gene Expression Assay

The bladder tissue, after being surgically removed, was immediately placed in a solution of 10% formalin in the procedure room. The tissue was fixed for a minimum of 6 hours but not more than 24 hours and paraffin embedded. Tissue sections (5 μm thick) were freshly cut from clinical blocks and mounted onto positively charged slides (Icahn School of Medicine at Mount Sinai IRB#15-1463). The slides were stored at 4°C until use. RNA was extracted from the tissue using the Qiagen RNeasy FFPE kit to test DV200, and samples with a DV200 of above 30% were profiled. A pathologist identified regions of interest (ROIs), including tumor, stromal, and immune cells, for each sample, ensuring they fit the 11mm x 11mm or 6.5mm x 6.5mm capture area on the Visium CytAssist (10X Genomics) slides. The tissue was deparaffinized, stained with H&E, and imaged at 4x magnification using an EVOS M7000 microscope to assess tissue structure and cellular morphology. The samples were then decrosslinked, hybridized with species-specific probes overnight (16-24 hours). Probes were ligated and released using the CytAssist instrument. Probes were captured by the CytAssist instrument from each sample onto a specialized visium slide with barcodes on the capture spots. We extended our probes on the visium slide and eluted in PCR tubes per sample to perform cDNA amplification, quantification, index PCR and clean-up steps using SPRIselect. Cycle numbers for our index PCR were determined by the qPCR QuantStudio

5 (Thermo Fisher Scientific, Waltham, MA, USA). Samples were cleaned using SPRIselect and post-library construction QC and quantification was performed with a D1000 Agilent Tapestation kit on the Agilent 4200 Tapestation system (Agilent, Santa Clara, CA, USA). Libraries were sequenced in paired end mode on a NovaSeq instrument (Illumina, San Diego, CA) targeting a depth of at least 275M reads per capture area. Sequencing data was filtered, aligned and quantified using the Space Ranger Software Suite (version 3.1, 10x Genomics) set to default parameters against the provided GRCh38 human reference genome. Space Ranger (10X Genomics) was used for genome alignment to GRCh38 human reference genome, creating a raw UMI count matrix. This was then created into a Seurat object using the R package, Seurat. Data was normalized using the SCTransform function. SpatialFeaturePlot was used to visualize the expression of individual genes across capture spots. Since each Visium spot covering multiple cells, we deconvoluted immune cell composition of each spot using the robust cell type decomposition (RCTD) algorithm(70) applying the spacexr R package (v.2.2.1). We also calculated enrichment score for the two gene signatures (Buffa hypoxia(71) and vasculature development(45)) for each Visium spot using AUCell(72) (v.1.32.0) R package. Seurat's SpatialFeaturePlot function was used to visualize the cell type deconvolution results by RCTD and pathway enrichment score by AUCell across capture spots. Softwares and packages used in this study are listed in **Table S5**.

Spatial localization of Mac and T cell subtypes and hypoxia signature

For a systematic examination of the spatial relationship between two Mac subtypes, aiding in the understanding of their roles in the TME, Pearson's correlation coefficient was calculated comparing the proportions of *SPP1*$^{+}$ and *CXCL9*$^{+}$ Macs. The analysis was performed independently for each sample to determine the spatial localization patterns of the two Mac subtypes. Statistical significance was determined using FDR-adjusted *p*-value, and significant correlations were indicated with asterisks. To allow for a comprehensive evaluation of the spatial

and statistical relationship between *SPP1*$^{+}$ Macs and hypoxia, proportions of *SPP1*$^{+}$ Macs and the hypoxia signature from AUCell were mapped spatially across tissue sections. A similar method was also applied for two macrophage subtypes vs. various T cell subtypes. A correlation between two continuous variables was examined using Pearson's method. For all analyses, statistical significance was set at two-tailed p-value < 0.05. All statistical analyses were conducted using R.

Neoadjuvant ICB-treated patient analysis

A subset of patients from scRNA-seq cohort is part of neoadjuvant pembrolizumab trial (n = 10). Responders and non-responders were classified according to the clinical definition of complete response based on RECIST v.1.1(73). The total number of cells for each cell type cluster was first calculated, followed by determining the proportions of *SPP1*$^{+}$ Macs and *CXCL9*$^{+}$ Macs within all Mac clusters.

Caris Study Cohort

FFPE samples from patients with UC (n=6,708) were submitted to a commercial CLIA-certified laboratory for molecular profiling (Caris Life Sciences, Phoenix, AZ) and analyzed by whole exome sequencing (WES), bulk RNA-seq, and IHC. The study follows guidelines provided by the Declaration of Helsinki, Belmont Report, and U.S. Common Rule. In accordance with compliance policy 45 CFR 46.101(b), this study was conducted using retrospective, de-identified clinical data, patient consent was not required, and the study was considered IRB exempt.

FFPE specimens underwent pathology review to measure percent tumor content and tumor size; a minimum of 10% of tumor content in the area for microdissection was required to enable enrichment and extraction of tumor-specific RNA. Qiagen RNA FFPE tissue extraction kit was used for extraction, and the RNA quality and quantity were determined using the Agilent TapeStation. Biotinylated RNA baits were hybridized to the synthesized and purified cDNA

targets, and the bait-target complexes were amplified in a post capture PCR reaction. The Illumina NovaSeq 6500 was used to sequence the whole transcriptome from patients to an average of 60M reads. Raw data was demultiplexed by Illumina Dragen BioIT accelerator, trimmed, counted, PCR-duplicates removed and aligned to human reference genome hg19 by STAR aligner(74) (v.2.7.8a). For transcription counting, TPM values were generated using the Salmon expression pipeline(75) (v.1.6.0).

Caris outcome data

Real-world OS information was obtained from insurance claims data and calculated from initiation of pembrolizumab to last contact while TOT was calculated from first to last of treatment time. Hazard ratio was calculated using the Cox proportional hazard models, and *p*-values were calculated using the log-rank test with significance determined as p-value of < 0.05.

Flow cytometry preparation and analysis

Cells were stained with LIVE/DEAD™ Fixable Aqua Dead Cell Stain Kit for viability (ThermoFisher, cat. # L34957) and F_c receptors were blocked using Human TruStain FcX™ (Biolegend, cat. # 422302) on ice in the dark for 20 minutes in FACS buffer (2% BSA, 1 mM EDTA in PBS). Surface molecules were stained in FACS buffer on ice in the dark for 25 minutes before washing. Cells were subsequently fixed and permeabilized utilizing CytoFix/CytoPerm reagents (BD, cat. #554714). Cells were stained for intracellular markers for an additional 25 minutes. Surface and intracellular flow antibodies used are detailed in **Table S5.** Cells were assessed using an Attune™ NxT Flow Cytometer (Thermo Fisher Scientific) and the Attune™ NxT Flow Cytometer Software (Thermo Fisher Scientific). Data was analyzed using FlowJo v10.5.3 (BD).

Upstream predictive ligand analysis

We performed upstream predictive ligand analysis using Ingenuity Pathway Analysis (IPA, Qiagen). DEG lists for *SPP1*$^+$ Macs versus *CXCL9*$^+$ Macs were uploaded with thresholds of $Log_2FC > 1$ and FDR-adjusted p-value < 0.05. The IPA core analysis function was used to identify upstream predictive ligands, with results reported as predictive z-scores.

Screen of upstream ligands on healthy donor blood monocyte-derived Macs

$CD14^+$ blood monocytes were bead isolated from HD PBMC using the Miltenyi Biotec human CD14 MicroBeads UltraPure kit (Miltenyi Biotec, cat. # 130-118-906). After isolation, flow cytometry was performed to confirm >90% $CD14^+$ purity to proceed. 100K monocytes per well were plated in flat-bottom 48-well plates at a density of 500K cells per mL in complete RPMI media [10% heat-inactivated fetal calf serum (FBS) (ThermoFisher, cat. #16000044), 1% Pen-Strep (ThermoFisher, cat. # 15140122), and 1% L-Glutamine (ThermoFisher, cat. # A2916801) in Gibco™ RPMI 1640 (ThermoFisher, cat. #11875-093)] with recombinant human (rh) M-CSF (50 ng/mL, Peprotech, cat. # 300-25) for 6 days. On day 3, half of the media was replenished with M-CSF at the same concentration. For the upstream ligand screen, on day 6, each of the skewing ligands were individually added to the existing media. Skewing ligands included ultrapure lipopolysaccharide (200 ng/mL, InvivoGen, cat. # tlrl-smlps), recombinant human (rh) TNF-α (20 ng/mL, Peprotech, cat. # 300-01A), rh IL-1β (20 ng/mL, Peprotech, cat. # 200-01B), phorbol 12-myristate 13-acetate (20 ng/mL, PMA, Sigma Aldrich, cat. # P1585-1MG), rh IFN-γ (20 ng/mL, Peprotech, cat. # 300-02), and rh EGF (100 ng/mL, Peprotech, cat. # AF-100-15). On day 7 this media was removed and replaced with fresh, plain complete RPMI. On day 8, monocyte-derived Macs and their cell-free supernatant were harvested. Supernatant was stored at -20C for later cytokine assessment using the flow-based LEGENDplex™ Human Macrophage/Microglia Panel (Biolegend, cat. #740502) assessing the cytokines: IL-12p70, TNF-α, IL-6, IL-4, IL-10, IL-1β, Arginase, CCL17(TARC), IL-1RA, IL-12p40, IL-23, IFN-γ, and CXCL10 (IP-10). Supernatant was also analyzed using the human CRP ELISA kit (R&D Systems, cat. # DCRP00), human IL-1β/IL-

1F2 QuicKit ELISA kit (R&D Systems, cat. # QK201), human IL-6 ELISA kit (ThermFisher, cat. #EH2IL6), and MIG/CXCL9 human ELISA kit (ThermoFisher, cat. # EHCXCL9). To assist with cell isolation from the plate, ice-cold 1 mM EDTA in PBS was added to each well and left on the plate, which was placed on ice for 30 mins. Cells were vigorously pipetted, without scraping the plate, and examined under the microscope to ensure their lifting from the plate. Cells were immediately stained for flow cytometry analysis.

Drug treatment of modelled SPP1⁺ Macs

To assess the effects of drugs abrogating IL-1β signaling on *SPP1⁺* Mac generation, we differentiated monocyte-derived Macs from primary peripheral blood monocytes from HDs with M-CSF over the course of 6 days, as described above. However, on day 6, macrophages were treated with CA-4948 (10 μM) (TargetMol, Cat. # T9027, CAS 1801344-14-8) versus an equivalent volume of vehicle DMSO or recombinant human IL1RA/IL-1RN (1 μg/mL) (Biolegend, cat. # 553906) versus an equivalent volume of vehicle PBS. Two hours later, cells were treated with IL-1β (20 ng/mL). On day 7, supernatant was removed, cells were washed with PBS, and on day 8, cells were lifted as described above for flow cytometry analysis, and supernatant was collected for further analysis with human IL-6 ELISA kit (Thermo Fisher Scientific).

Cell lines

Human monocyte cells (THP-1, ATCC, TIB-202, RRID: CVCL_0006) were cultured in complete RPMI, as previously described. NY-ESO-1 specific Jurkat 76 T cells were created by using TCR αβ-negative Jurkat 76 T cells (76) obtained from Prof. Mirjam Heemskerk, Department of Hematology, Leiden University, transduced with NY-ESO-1-specific TCR(77) obtained from Prof. Antoni Ribas, Tumor Immunology Program, University of California Los Angeles and cultured in complete RPMI. All cell cultures were incubated at 37°C with a humidified atmosphere with 5%

CO_2. Human cell lines were authenticated via short tandem repeat analysis. Cells were tested for *Mycoplasma* within 1 month before using.

Hypoxia treatment of THP-1 monocyte-derived Macs

Macs were grown from human THP-1 cells plated in complete RPMI at 2.5e5 cells/well in 48-well plates. On day 0, 150 nM PMA (Sigma Aldrich, cat. # P1585-1MG) was added to THP-1 cells to initiate Mac differentiation. On day 3, these resultant Macs were treated with IL-1β (20 ng/mL). On day 4, the macrophages were washed with PBS, media was replaced, and the Macs were added to either hypoxia (1% O_2) or normoxia (21% O_2) conditions for two days. To establish hypoxic conditions, the culture plate was encapsulated in a plastic pouch with an O_2 scavenger pack and meter to measure O_2 levels as part of the nBionix hypoxic cell culture kit (Bulldog Bio). Once the O_2 levels fell to 1%, the culture plate was clamped from the O_2 scavenger pack and placed in an incubator. On day 6, Macs were assessed for CLEC5A and TREM1 surface expression via flow cytometry.

Bulk RNA-seq and RT-qPCR of IL-1β- stimulated Macs

Macs were cultured from HD blood monocytes plated as described in the previous section but in 6-well plates at the same density but at $1e^6$ cells/well to obtain sufficient RNA material. For bulk RNA-seq, Macs treated with IL-1β (20 ng/mL) were compared to untreated Macs. Upon culture with skewing agents for 24h, total RNA was isolated using Trizol (Invitrogen) and the Direct-zol RNA Microprep Kit (Zymo Research, cat. # R2060). For bulk RNA-seq, poly A selection was then performed to isolate mRNA, which was sequenced at 50 base pair (bp) single reads for 50 million total reads. Reads were aligned to the GRCh37 human genome. DEseq2 was used to determine DEGs. For RT-qPCR, total RNA was assessed using Nanodrop (Thermo Scientific, Waltham, MA, USA) then converted to cDNA using the cDNA EcoDry Premix Double Primed kit (Clontech, cat. # 639549) as per manufacturer instructions, and then assessed for expression of select genes

using probe-based Taqman primers as detailed in **Table S5**, the TaqMan Fast Advanced Master Mix (ThermoFisher, cat. # 4444556), and the CFX384 Touch Real-Time PCR Detection System (BIO-RAD). Relative gene expression was quantified using the ΔΔCt (Delta-Delta Ct) method, with *HPRT1* (encoding hypoxanthine phosphoribosyltransferase 1) as the housekeeping gene, given its low but consistent expression across somatic tissues.

Bulk RNA-seq of IFNγ- stimulated Macs

Macs were cultured from blood monocytes at $1e^6$ cells/well as described in the previous section. Macs treated with IFNγ (40 ng/mL) were compared to a vehicle control of PBS with 0.1% BSA, which is what IFNγ was stored in for 48 hours. Total RNA was isolated with Trizol (Invitrogen) and the Direct-zol RNA Microprep Kit (Zymo Research, cat. # R2060). For bulk RNA-seq, poly A selection was applied to isolate mRNA, which was then sequenced at 30 million total reads. Reads were aligned to the GRCh38 human genome. DEseq2 was utilized to determine DEGs.

Whole-slide multiplex imaging analysis at single-cell resolution with MARQO

For the analysis of consecutive slides, we adapted our open-source, user-guided automated pipeline(57). MARQO streamlines start-to-finish, single-cell resolution analysis of whole-slide tissue, named multiplex-imaging analysis, registration, quantification and overlaying. The pipeline is deployed via Singularity container, building on TensorFlow's prebuilt images with a Python virtual environment containing all required libraries. The users specify the imaging modality and initiate tissue masking, registration, tiling, and color deconvolution on the fly; while automated, these steps remain user-modifiable to ensure quality control. Tissue masking can be adjusted by manually defining regions, tiling is set at a default of 1,000 × 1,000 pixels (~500 µm × 500 µm) with customizable overlap and exclusion criteria, and HistomicsTK-based color deconvolution dynamically extracts three channels (chromogen, hematoxylin, residual). Configuration files preserve stepwise reproducibility. In the reviewing tab, users classify clusters, stitch registered

whole-slide images, reconcile compartment annotations from standardized geojson files (currently created in QuPath), and generate summary tables linking cell identity with tissue compartments. Visualizations of marker-defined subsets, quantification, and density metrics are supported, and outputs can be exported to third-party formats for further analysis. MARQO's whole-slide registration module first performs translational alignment of thumbnail images, then uses overlapping tiles (10%) to preserve edge integrity and SimpleElastix-based affine and elastic registrations optimized on images. Nuclear counterstains extracted during dynamic deconvolution serve as the alignment anchor across stains, and vector fields are applied to RGB channels for cell-resolution registration. Segmentation is performed CellPose. In the quantification module, nuclear masks are expanded to approximate cytoplasmic regions, and pixel-level and morphological metadata (intensity distributions, area, perimeter, axes, nuclear staining intensity) are extracted per cell, with duplicates avoided by restricting measurements to nuclei within tile bounds. Metadata are appended into a features table spanning all stains and cells, and MARQO also produces geojson spatial files of segmented objects.

To assess spatial localization of $CD8^+$ cells with $SPP1^+$ $CD68^+$ and HLA-DR^+ $CD68^+$ Macs, spatial graphs were constructed using all aligned cell centroids within each tissue section. A k-nearest neighbor (k-NN) graph (k=8) was built on the fixed reference section and partitioned using the Leiden algorithm. Cells from all sections were then assigned to these neighborhoods based on their aligned coordinates. For each Leiden neighborhood, a spatial graph was then built only for the target cells, and the average distance between them was calculated. The average distances across all neighborhoods were used to compare cell dispersions associated with response. For estimating the difference between HCRN GU 14-182 responder and non-responder, we compared the distributions using the Kolmogorov-Smirnov test.

To investigate cell type frequency differences associated with response, we calculated cell type frequencies independently for each neighborhood and each section, as marker co-expression can only be determined within the same tissue section where markers are simultaneously stained. Single-marker and multi-marker co-expression frequencies were computed as the percentage of cells positive for the marker(s) relative to the total number of cells in that neighborhood-section combination. To compare functional macrophage subsets across tissue depth, we calculated cell type ratios by dividing the count of one cell type in a given section by the count of another cell type in a different section within the same neighborhood. For comparison between HCRN GU 14-182 responder and non-responder, we tested differences in neighborhood-level frequencies and ratios using two-tailed independent Student's t-tests, excluding low-confidence neighborhoods (<50 cells). Outliers above the 90th percentile were capped for visualization only; statistical analyses used uncapped values.

Co-culture of in vitro *modelled Macs and CD8⁺ and CD4⁺ T cells*

Macs were derived from monocytes isolated from HD peripheral blood and cultured at a density of 500K cells/mL with M-CSF (50 ng/mL) for six days. They were then polarized with either IL-1β (20 ng/mL) or IFNγ (40 ng/mL) for an additional 24 hours. In relevant experiments, Macs were pre-treated with CA-4948 (10 μM) or an equivalent volume of DMSO for two hours before IL-1β stimulation. On day 7, Macs were detached by adding ice-cold 1 mM EDTA in PBS to each well and incubating on ice for 30 minutes. Cells were gently pipetted without scraping to ensure detachment, which was confirmed under a microscope. Concurrently, naïve $CD8^+$ or $CD4^+$ T cells were isolated from the same HD using the EasySep™ Human Naïve $CD8^+$ T cell Isolation Kit (STEMCELL Technologies, cat. # 19258) or $CD4^+$ T Cell Isolation Kit (STEMCELL Technologies cat. #19555). Once both Macs and T cells were isolated and counted, 100K Macs and 100K T cells were co-cultured in 1.5 mL of cRPMI in 24-well plates. Each Mac subset (IL-1β-stimulated or IFNγ-stimulated) was co-cultured with either $CD8^+$ or $CD4^+$ T cells. Human IL-2 (Peprotech,

cat. #200-02) was added at a final concentration of 50 IU per well, and Dynabeads™ Human T-Activator CD3/CD28 for T cell Expansion and Activation (Gibco, cat. # 11131D) were included at 12.5 µL per million T cells. On day 10, Dynabeads were removed using a magnetic separator, and cells were centrifuged at 500g for 5 minutes at room temperature. The supernatant was discarded, and 250 µL of fresh stimulation media was added per well. This media contained, per 1 mL, 0.2 µL PMA, 1 µL ionomycin, 1 µL GolgiPlug, and 0.67 µL GolgiStop. Cells were incubated in this stimulation media for six hours before being harvested for flow cytometry analysis to assess T cell function.

Tocilizumab treatment during macrophage and CD8⁺ T cells co-culture

For experiments assessing IL-6 blockade, co-cultures of IL-1β–stimulated macrophages and naïve CD8⁺ T cells were established as described earlier. At the time of CD8⁺ T cell addition to macrophages, either tocilizumab (100 ng/mL, Selleck Chemicals, cat. # A2012) or Ultra-LEAF™ Purified Human IgG1 Isotype Control antibody (100 ng/mL, Biolegend, cat. # 403501) was added to the wells. All subsequent culture conditions and flow cytometry analyses were performed as outlined in the co-culture protocol.

Antigen-specific T-cell activation co-culture assay with in vitro *modelled Macs*

THP-1 cells were differentiated into macrophages by culturing at a density of 750K cells/mL in complete RPMI in a 6-well plate and treating with 150 nM PMA (Sigma Aldrich, cat. # P1585-1MG) for 48 hours. Cells were then polarized for 24 hours with either 20 ng/mL IL-1β (to model *SPP1*⁺-like macrophages) or 40 ng/mL IFNγ (to model *CXCL9*⁺-like macrophages). After polarization, macrophages were lifted using 1 mM EDTA in PBS at 37°C, washed, and pulsed with 10 µg/mL NY-ESO-1 peptide at a concentration of $1e^6$ cells/mL for 3 hours at 37°C. NY-ESO-1–specific Jurkat 76 T cells were added to macrophages at a 1:1 ratio (100K Macs and 100K T

cells) and co-cultured for 24 hours in 200 uL total in a 96-well plate. T-cell activation was assessed by flow cytometry using antibodies against CD25 and CD69 (BioLegend). Macrophage expression of HLA class I molecules following IL-1β or IFNγ skewing was evaluated in parallel by staining with anti-HLA-A/B/C antibody (Biolegend).

Assessment of IL-6, IL-1β, SPP1, and CRP on naïve CD8⁺ and CD4⁺ T cells' differentiation into cytotoxic effector cells

Human naïve CD8⁺ or CD4⁺ T cells were isolated from HD PBMC using the EasySep™ Human Naïve CD8⁺ T cell or CD4⁺ T cell Isolation Kits (STEMCELL technologies), respectively. Naïve CD8⁺ or CD4⁺ T cells were plated in complete RPMI at a density of $1e^6$ cells/mL in 96 well plates. rhIL-2 (Peprotech, cat. #200-02) was added to CD8⁺ T cells at 50 international units (I.U.). rhIL-6 (10 ng/mL, Peprotech, cat. # 200-06), rhIL-1β (10 ng/mL, Peprotech, cat. # 200-01B), rhSPP1 (10 ng/mL,Peprotech, cat. # 120-35), or rhCRP (10 ng/mL, Invitrogen, cat. # RP75528) was added to select treatment wells as specified. CD8⁺ T cells were activated for 24h using Dynabeads™ Human T-Activator CD3/CD28 for T cell Expansion and Activation (Gibco) as per manufacturer protocols. After 24h, beads were magnetically removed. On Day 5, the T cells were re-stimulated for 6 hours with PMA (50 ng/mL, Sigma Aldrich, cat. # P1585-1MG) and ionomycin calcium salt from *Streptomyces conglobatus* (1 ug/mL, Sigma Aldrich, cat. # I0634, CAS 56092-82-1) with Protein Transport Inhibitor containing Monensin (Fisher/BD, cat. # 554724), GolgiStop™ (Fisher/BD), as per manufacturer instructions. T cells were then harvested and stained for flow cytometry analysis.

Bulk RNA-seq of CD8⁺ T and CD4⁺ T cells

Human naïve CD8⁺ or CD4⁺ T cells were isolated as described in the previous section and plated in 6-well plates at a density of $1e^6$ cells/mL. T cells were cultured with rhIL-6 (10 ng/mL, Peprotech) for 4 hours with or without plate-coated functional grade monoclonal CD3 eBioscience™ (10

ug/mL, clone: OKT3, ThermoFisher, cat. # L34957, RRID: AB_468855) and soluble mouse anti-human CD28 (2.5 ug/mL, Fisher/BD, cat. # 555726, RRID: AB_396069). After 4 hours, total RNA was isolated using Trizol (Invitrogen, cat. # 15596026) and the Direct-zol RNA Microprep Kit (Zymo Research, cat. # R2060). For bulk-RNA-seq, poly A selection was then performed to isolate mRNA, which was sequenced at 50 base pair (bp) single reads for 50 million total reads. Sequences were aligned to genes using the GRCh38 human reference genome. DEseq2 was applied to calculate DEGs.

Plasma co-culture with T cells

Previously processed and frozen patient and HD plasma was thawed and spun at 2,000g for 10 mins at 4C to remove debris before plating. T cells were isolated from HD PBMC using the Pan T Cell Isolation Kit (Miltenyi Biotec, cat. # 130-096-535) and following manufacturer instructions. Using a 96 flat-bottom plate, pan T cells were plated at 100K cells/well at a 1e6 cell/mL density with 100 uL of either plasma from patients with UC or HDs. rhIL-2 (Peprotech, cat. #200-02) was added at 50 I.U. per well. Cells were cultured for 24h with plasma before harvesting and flow cytometry staining. Six hours before cell harvest, T cells were spun down and half of the plasma (50 uL) was removed and replaced with fresh RPMI media with added Protein Transport Inhibitor (Containing Monensin), GolgiStop™ (Fisher/BD), as per manufacturer instructions. Cells were then harvested and stained for flow cytometry.

RESOURCE AVAILABILITY:

Lead contact:

More information and requests for resources and reagents should be directed to the lead contacts and corresponding authors, Dr. Diego Chowell (diego.chowell@mssm.edu), Dr. Matthew Galsky (matthew.galsky@mssm.edu) and Dr. Nina Bhardwaj (nina.bhardwaj@mssm.edu).

Materials availability:

This study did not generate unique new reagents or biological materials.

Data and code availability:

scRNA-seq, Visium spatial data, and bulk RNA-seq and are publicly available and have been deposited on Zenodo, accessible at this link: https://doi.org/10.5281/zenodo.18237374. Any information required to re-analyze the data reported in this paper is available form the lead contact upon request.

References:

1. Sharma P, Allison JP. The future of immune checkpoint therapy. Science 2015; 348:56–61.
2. Balar AV, Galsky MD, Rosenberg JE, Powles T, Petrylak DP, Bellmunt J, et al. Atezolizumab as first-line treatment in cisplatin-ineligible patients with locally advanced and metastatic urothelial carcinoma: a single-arm, multicentre, phase 2 trial. The Lancet 2017;389:67–76.
3. Balar AV, Kulkarni GS, Uchio EM, Boormans J, Mourey L, Krieger LEM, et al. Keynote 057: Phase II trial of Pembrolizumab (pembro) for patients (pts) with high-risk (HR) nonmuscle invasive bladder cancer (NMIBC) unresponsive to bacillus calmette-guérin (BCG). JCO 2019;37:350–350.
4. Bellmunt J, de Wit R, Vaughn DJ, Fradet Y, Lee J-L, Fong L, et al. Pembrolizumab as Second-Line Therapy for Advanced Urothelial Carcinoma. New England Journal of Medicine 2017;376:1015–26.
5. Katz H, Wassie E, Alsharedi M. Checkpoint inhibitors: the new treatment paradigm for urothelial bladder cancer. Medical Oncology. Springer US; 2017;34:1–11.
6. Powles T, O'Donnell PH, Massard C, Arkenau HT, Friedlander TW, Hoimes CJ, et al. Efficacy and safety of durvalumab in locally advanced or metastatic urothelial carcinoma: Updated results from a phase 1/2 open-label study. JAMA Oncology 2017;3:1–10.
7. Sharma P, Retz M, Siefker-Radtke A, Baron A, Necchi A, Bedke J, et al. Nivolumab in metastatic urothelial carcinoma after platinum therapy (CheckMate 275): a multicentre, single-arm, phase 2 trial. The Lancet Oncology 2017;18:312–22.
8. Patel MR, Ellerton J, Infante JR, Agrawal M, Gordon M, Aljumaily R, et al. Avelumab in metastatic urothelial carcinoma after platinum failure (JAVELIN Solid Tumor): pooled results from two expansion cohorts of an open-label, phase 1 trial. The Lancet Oncology 2018;19:51–64.

69. Krishna C, Tervi A, Saffern M, Wilson EA, Yoo S-K, Mars N, et al. An immunogenetic basis for lung cancer risk. Science 2024;383:eadi3808.
70. Cable DM, Murray E, Zou LS, Goeva A, Macosko EZ, Chen F, et al. Robust decomposition of cell type mixtures in spatial transcriptomics. Nat Biotechnol 2022;40:517–26.
71. Di Giovannantonio M, Hartley F, Elshenawy B, Barberis A, Hudson D, Shafique HS, et al. Defining hypoxia in cancer: A landmark evaluation of hypoxia gene expression signatures. Cell Genomics 2025;5:100764.
72. Aibar S, González-Blas CB, Moerman T, Huynh-Thu VA, Imrichova H, Hulselmans G, et al. SCENIC: single-cell regulatory network inference and clustering. Nat Methods 2017;14:1083–6.
73. Eisenhauer EA, Therasse P, Bogaerts J, Schwartz LH, Sargent D, Ford R, et al. New response evaluation criteria in solid tumours: Revised RECIST guideline (version 1.1). European Journal of Cancer 2009;45:228–47.
74. Dobin A, Davis CA, Schlesinger F, Drenkow J, Zaleski C, Jha S, et al. STAR: ultrafast universal RNA-seq aligner. Bioinformatics 2013;29:15–21.
75. Patro R, Duggal G, Love MI, Irizarry RA, Kingsford C. Salmon provides fast and bias-aware quantification of transcript expression. Nat Methods 2017;14:417–9.
76. Rosskopf S, Leitner J, Paster W, Morton LT, Hagedoorn RS, Steinberger P, et al. A Jurkat 76 based triple parameter reporter system to evaluate TCR functions and adoptive T cell strategies. Oncotarget 2018;9:17608–19.
77. Gschweng EH, McCracken MN, Kaufman ML, Ho M, Hollis RP, Wang X, et al. HSV-sr39TK Positron Emission Tomography and Suicide Gene Elimination of Human Hematopoietic Stem Cells and Their Progeny in Humanized Mice. Cancer Research 2014;74:5173–83.

Figure Legends:

Figure 1. Schematic overview of our study design. Created with BioRender.com.

Figure 2. Association of plasma CRP with OS in patients with mUC.

(A) OS probability of patients with mUC stratified by quartiles of baseline CRP levels in four clinical trials. The quartile groups were defined using data from all treatment arms within each trial. Cohorts 1 and 2 of IMvigor210 were assessed together and separately. Two-sided *p*-values were determined using the log-rank test. **(B)** OS probability of patients with mUC stratified by on-treatment changes in CRP levels in three clinical trials. Upper quartile (Q4) vs. the remainder (Q1-Q3) was used to dichotomize samples into Low and High. On-treatment changes were displayed

using the ratio of CRP level on day 1 of treatment cycle 3 (IMvigor210 and IMvigor130) or day 1 of cycle 4 (IMvigor211) to the baseline level. Cohorts 1 and 2 of IMvigor210 were assessed together and separately. Patients were dichotomized at the median CRP ratio calculated across all treatment arms within each trial. Two-sided *p*-values were determined using the log-rank test.

Figure 3. Relationship between baseline plasma CRP and IL-6 in patients with mUC.

(A) Correlation between baseline CRP and 92 O-link analytes in the HCRN GU14-182 cohort. Red and blue dots indicate statistically significant positive and negative correlations, respectively. **(B)** Heatmap of the 10 analytes most strongly correlated with baseline CRP, displayed in z-scores. CRP groups are categorized based on quartile values. **(C)** Scatter plot showing the positive correlation between baseline CRP and IL-6 in the IMvigor210 cohort. **(D)** Volcano plot showing DEGs between the IL-6 high (Q4) and low (Q1) groups in the IMvigor210 cohort. **(E)** GSOA using the DEGs between IL-6 high (Q4) and IL-6 low (Q1) groups based on Hallmark gene sets in the IMvigor210 cohort. **(F)** Stacked bar chart showing the distribution of UC subtypes across IL-6 quartile groups in the IMvigor210 cohort. **(G-H)** OS probability of patients with mUC in the IMvigor210 and HCRN GU14-182 trials stratified by quartile of IL-6 levels, with Q4 being the highest and Q1 the lowest. **I.** RNAscope quantitative whole slide image analysis using the HALO AI ISH module. Representative fields of view from two HCRN GU14-182 baseline specimens probed for *IL6* RNAscope (green), deconvolution, object phenotyper for cellular detection of stroma/immune (green) and tumor cells (red), and mark-up of positive expressing cells is shown. **(J-K)** Scatter plots showing positive correlations between *IL6* RNAscope H-score with O-link plasma IL-6 and CRP in the HCRN GU14-182 trial. **(L)** *IL6* RNAscope quantitative whole slide image analysis (n = 10) of the fraction of *IL6* copies per cell group in the HCRN GU14-182 trial. Mann–Whitney *U* test was performed (**p<0.01).

Figure 4. Multi-transcriptomics characterization of *SPP1*$^+$ Mac and *CXCL9*$^+$ Macs in UC. **(A)** UMAP of 50 tumors and 6 paired adjacent-normal tissues from patients with UC revealing 40 different cell types from scRNA-seq. **(B)** GSEA using marker genes for each cell type identified from the scRNA-seq data from panel **(A)**, with a $\log_2$FC-ranked gene list based on IL-6 Q1 vs. Q4 comparison from bulk RNA-seq of IMvigor210 (**Figure 3D**). **(C)** Scatter plot of *SPP1* and *CXCL9* expression in Mac subtypes. The contingency table displays the number of cells expressing or lacking *SPP1* (*SPP1*+ or *SPP1*-), and their respective classification based on *CXCL9* expression (*CXCL9*+ or *CXCL9*-). An odds ratio of 0.65 (two-sided Fisher's exact test p<0.0001) suggests mutually exclusive expression. **(D)** Volcano plot showing DEGs between *CXCL9*$^+$ Macs and *SPP1*$^+$ Macs. **(E)** GSOA using DEGs between *CXCL9*$^+$ Macs and *SPP1*$^+$ Macs based on Hallmark gene sets. **(F)** Representative matched fields of view from HCRN GU14-182 baseline specimens stained for RNAscope and mIHC. Consecutive slides were stained for *IL6* RNAscope (pink) and CD68 IHC (yellow) (left panel) and mIHC for SPP1 (brown), CD68 (green) and HLA-DR (purple) (right panel). Red boxes indicate the same *IL6* and SPP1 expressing Macs on the consecutive slides. **(G)** Consecutive slides were stained for *CXCL9* RNAscope (pink) and CD68 IHC (yellow) (left panel) and mIHC for SPP1 (brown), CD68 (green) and HLA-DR (purple) (right panel). Blue boxes indicate the same *CXCL9* and HLA-DR expressing Macs on the consecutive slides. **(H)** Representative image of the spatial organization of *CXCL9*$^+$ Macs, *SPP1*$^+$ Macs, and hypoxia signatures from Visium spatial transcriptomics from the HCRN GU14-182 trial. The hypoxia signature was evaluated using the Hallmark gene sets. *CXCL9*$^+$ Macs and *SPP1*$^+$ Macs exhibit distinct spatial segregation, and *SPP1*$^+$ Macs show strong spatial co-localization with the hypoxia transcriptional signature. **(I)** Dot-plots summarizing the spatial organization of the *CXCL9*$^+$ Macs, *SPP1*$^+$ Macs, and hypoxia signatures among 13 bladder tumors from the HCRN GU14-182 trial. A stronger negative correlation between *SPP1*$^+$ Macs and *CXCL9*$^+$ Macs with increasing CRP levels and an overall positive correlation between *SPP1*$^+$ Macs and the hypoxia signature were observed. **(J)** scRNA data showing the *CXCL9*$^+$ Macs to *SPP1*$^+$ Macs ratio according to the clinical

complete response of patients with muscle-invasive bladder cancer (MIBC) from the neoadjuvant pembrolizumab cohort (HCRN GU20-444). **(K)** OS probability of 337 patients with UC treated with atezolizumab in IMvigor210, comprising 187 patients with primary tumors and 150 patients with metastatic lesions, stratified by quartiles of the *CXCL9:SPP1* ratio calculated from bulk RNA-seq of the corresponding primary or metastatic samples. **(L)** Distribution of *CXCL9:SPP1* ratios from bulk RNA-seq of primary tumors (n=187 distinct patients) vs. metastatic lesions (n=150 distinct patients) from IMvigor210. **(M)** OS probability of patients with metastatic UC lesions treated with pembrolizumab from Caris Life Sciences RWD split by quartiles of *CXCL9:SPP1* ratio calculated from bulk RNA-seq of metastatic sites.

Figure 5. *SPP1*$^+$ Macs are enriched in the tumor and are polarized by IL-1β, whereas *CXCL9*$^+$ Macs are driven by IFNγ.

(A) Frequencies of tumor Mac populations between tumor versus no-evidence-of-disease (NED) and normal-adjacent tissue. **(B)** CLEC5A and TREM1 expression by Macs from normal-adjacent and tumor tissue from a representative treatment-naïve MIBC patient. **(C)** CLEC5A and TREM1 expression between matched tumor and normal-adjacent tissue from 6 patients with treatment-naïve MIBC. **(D)** IL-1β drives CLEC5A and TREM1 upregulation in Macs differentiated from blood monocytes from a representative HD. US: unstimulated condition. **(E)** IL-1β drives the upregulation of CLEC5A and TREM1 individually and **(F)** combined in monocyte-derived Macs (n=11 HDs). **(G)** Bulk RNA-seq of monocyte-derived Macs +/- IL-1β (n=2 HDs). **(H)** Relative expression of *CLEC5A, TREM1, SPP1, IL1B, IL6,* and *C1QC* from monocyte-derived Macs +/- IL-1β (n=8 HDs). **I.** IL-1β increases the secretion of IL-6 in monocyte-derived Macs (n=11 HDs). **(J)** IFNγ treatment decreases CLEC5A$^+$TREM1$^+$ expression and **(K)** increases CXCL9 secretion in monocyte-derived Macs (n=11 HDs). **(L)** Bulk RNA-seq of monocyte-derived Macs +/- IFNγ (n=3 HDs). **(M)** Treatment of IL1RA (1 μg/mL) prior to IL-1β-skewing decreases CLEC5A$^+$TREM1$^+$

cells. **(N)** CA-4948 treatment prevents IL-1β driven upregulation of *CLEC5A, TREM1, SPP1, IL1B,* and *IL6*; increases *C1QC* expression; and **(O)** prevents IL-6 secretion. Wilcoxon signed-rank tests were performed (*p<0.05; **p<0.01; ***p<0.001).

Figure 6. In vitro co-culture reveals immunosuppressive effects of *SPP1*$^+$ Macs on CD8$^+$ and CD4$^+$ T cells.

(A) Representative flow of naïve CD8$^+$ T cells co-cultured with IL-1β-skewed (*SPP1*$^+$ like*)* Macs and IFNγ-skewed (*CXCL9*$^+$ like*)* Macs. **(B-D)** IL-1β-skewed Macs reduce IFNγ, TNFα, and granzyme B production in CD8$^+$ T cells. **(E-F)** IL-1β-skewed Macs suppress CD8$^+$ T cell proliferation, as shown by CFSE staining. **(G-H)** CA-4948 treatment of IL-1β-skewed Macs in co-culture decreases CD8$^+$ T cell production of IFNγ, TNFα, and granzyme B compared to treatment with a DMSO control. **(I)** Representative flow of naïve CD4$^+$ T cells co-cultured with IL-1β-skewed and IFNγ-skewed Macs. **(J-K)** IL-1β-skewed Macs reduces IFNγ and granzyme B but not TNFα production in CD4$^+$ T cells. **(L)** *SPP1*$^+$ Macs exhibit negative spatial co-localization with CD4$^+$ and CD8$^+$ T cells, whereas *CXCL9*$^+$ Macs show positive co-localization, based on Visium spatial transcriptomics on 13 tumors from the HCRN GU14-182.

Figure 7. IL-6, produced by SPP1$^+$ Macs, suppresses the differentiation of CD8$^+$ and CD4$^+$ effector T cells.

(A-B) Tocilizumab treatment of IL-1β-skewed Macs in co-culture decreases CD8$^+$ T cell production of IFNγ and TNFα compared to treatment with a hIgG1 control**. (C)** Representative flow plot and **(D)** summative graphs of cytolytic granule production by naïve CD8$^+$ T cells activated by CD3/CD28 coated Dynabeads^{TM} and re-stimulated with PMA and ionomycin +/- IL-6 for 5 days.

(E-F) Repeat of C and D in naïve $CD4^+$ T cells. Wilcoxon signed-rank tests were performed (*p<0.05; **p<0.01; ***p<0.001). **(G)** Bulk RNA-seq of naïve $CD8^+$ T cells cultured +/- IL-6 **H)** with activation with plate-coated anti-CD3 and CD28. **(I-J)** Repeat of **G** and **H** in $CD4^+$ T cells. **(K)** Expression of genes related to IL-6 signaling and T cell function by circulating naïve $CD8^+$ T and **(L)** $CD4^+$ T cells from scRNA-seq of 9 PBMC samples from patients with UC. Average gene expressions were calculated for high, medium, and low IL-6 groups (n=3 patients each). **(M)** Frequency of $SOCS3^+$ cells after 24-hour culture of T cells with plasma from HDs versus patients with UC, gated on $CD8^+$ T cells and **(N)** $CD4^+$ T cells. Mann-Whitney *U* test was performed (**p<0.01; ***p<0.001). **(O)** Associations of plasma IL-6 concentrations versus % $SOCS3^+$ $CD8^+$ T cells and **(P)** versus $SOCS3^+$ $CD4^+$ T cells between UT and IL-6 (10 ng/mL) as well as HD and UC plasma conditions. Pearson correlation coefficients (r) and p-values were calculated.

Figure 1

Clinical trial cohorts of metastatic urothelial cancer

Atezolizumab

IMvigor210 (n=406)

IMvigor211 (n=436)

IMvigor130 (n=331)

Pembrolizumab

HCRN GU14-182 (n=80)

Multi-transcriptomic analyses (bulk, single-cell, and spatial transcriptomics)

Urothelial tissue (MSSM, n=45) + Urothelial tissue (Chen *et al.*, n=11) = Integrated scRNA cohort (n=153,624 cells)

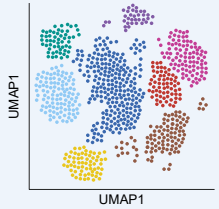

Pre-treatment plasma CRP

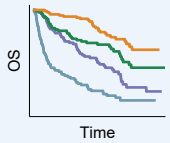

High CRP → Poorer outcome

On-treatment plasma CRP dynamics

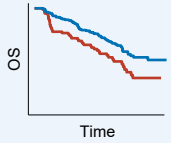

Large on-treatment decline → Better outcome

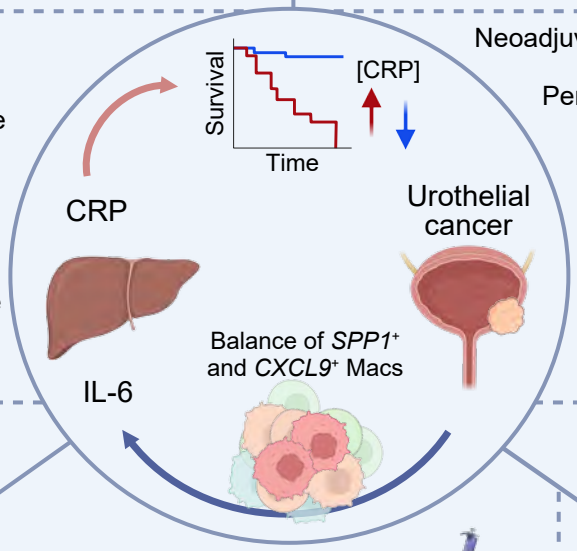

Neoadjuvant pembrolizumab: HCRN GU20-444 (scRNA; n=30)
Atezolizumab: IMvigor210 (bulk; n=337)
Pembrolizumab: Caris real-world data (bulk; n=422)

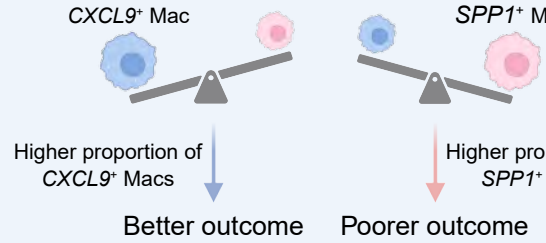

Plasma IL-6 positively correlates with CRP and tumors enriched in *SPP1*⁺ Macs

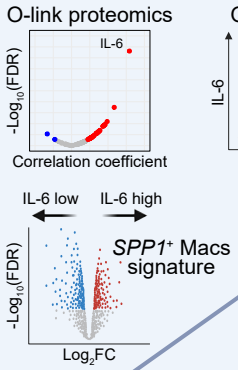

In vitro validation

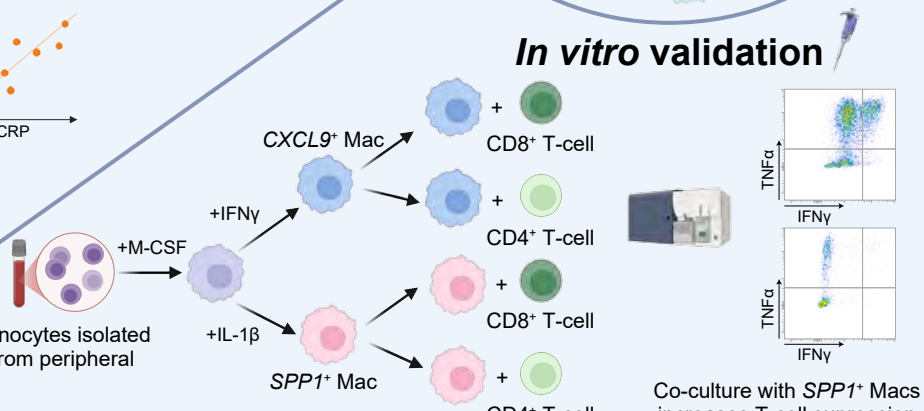

Co-culture with *SPP1*⁺ Macs increases T-cell supression

13 patients from HCRN GU14-182

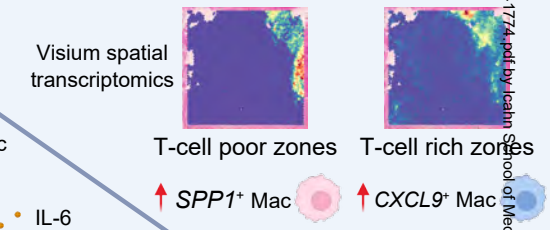

Distant spatial distribution of *SPP1*⁺ and *CXCL9*⁺Macs in metastatic urothelial cancer

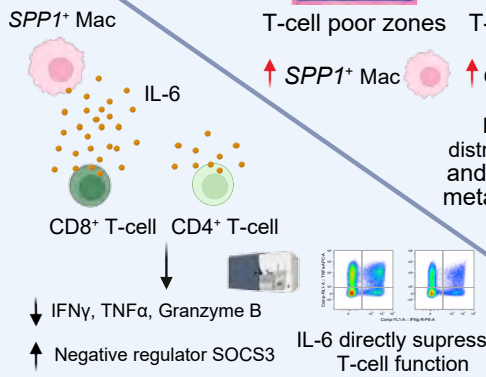

IL-6 directly supresses T-cell function

Figure 2

A Baseline CRP and OS

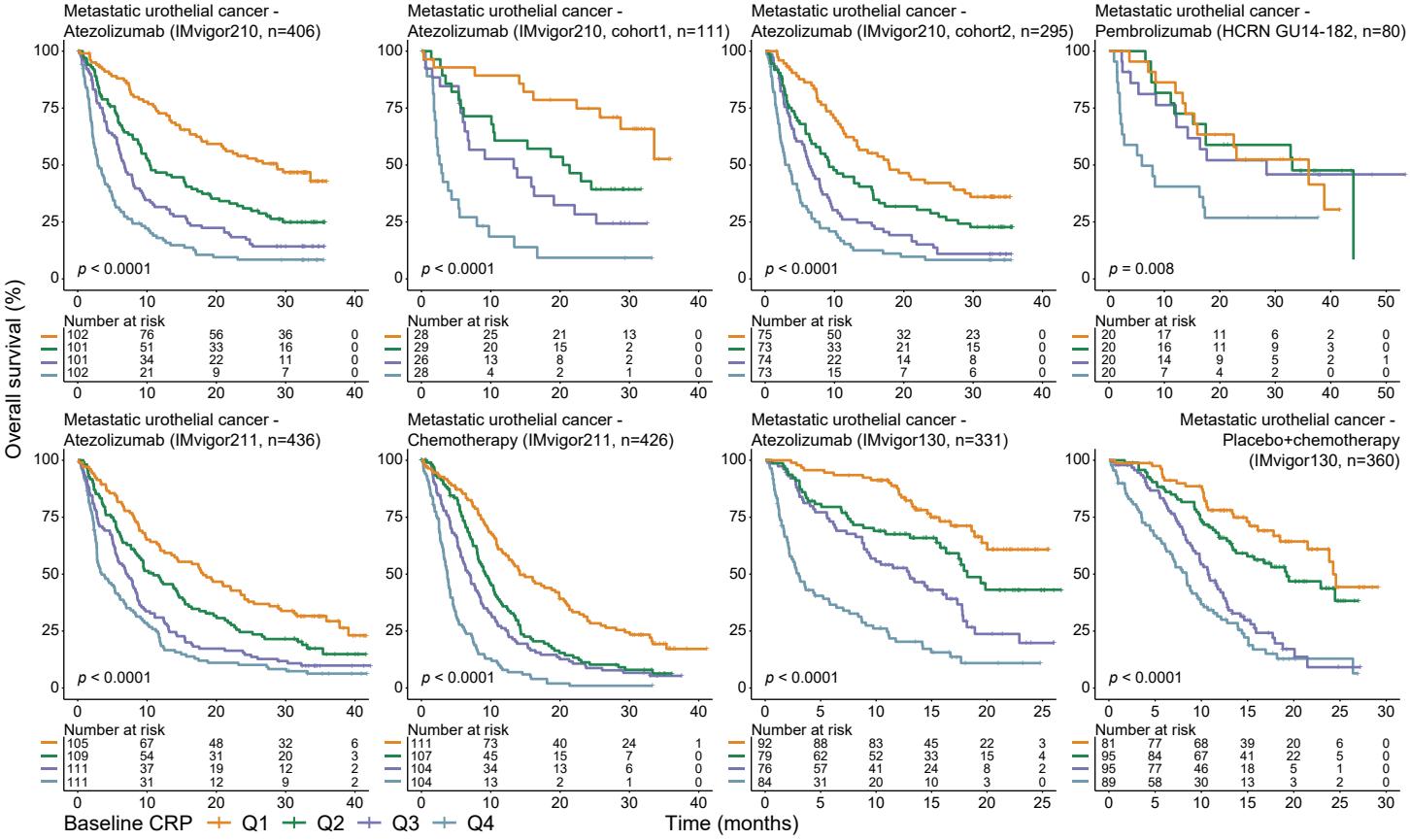

B On-treatment change in CRP and OS

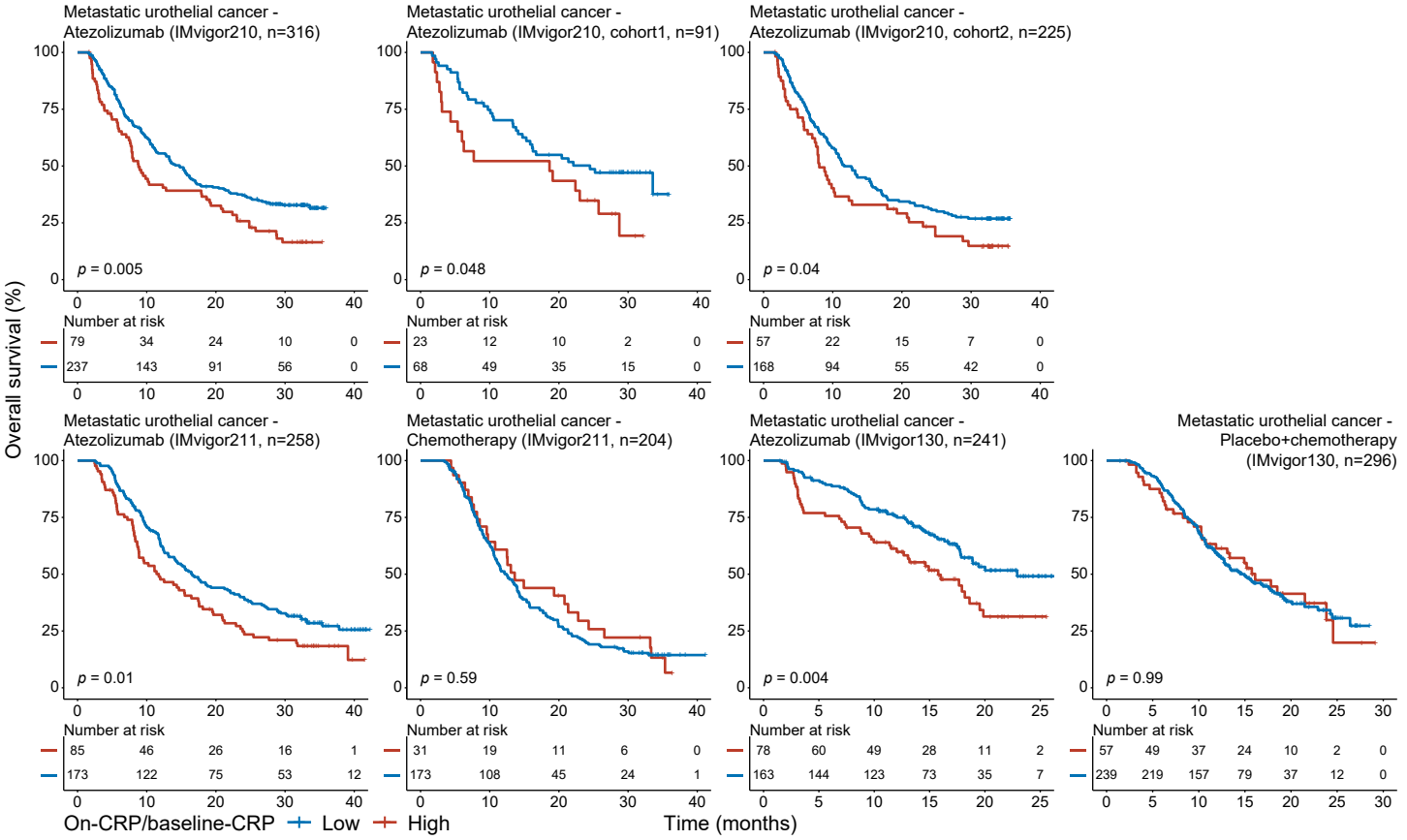

Figure 3

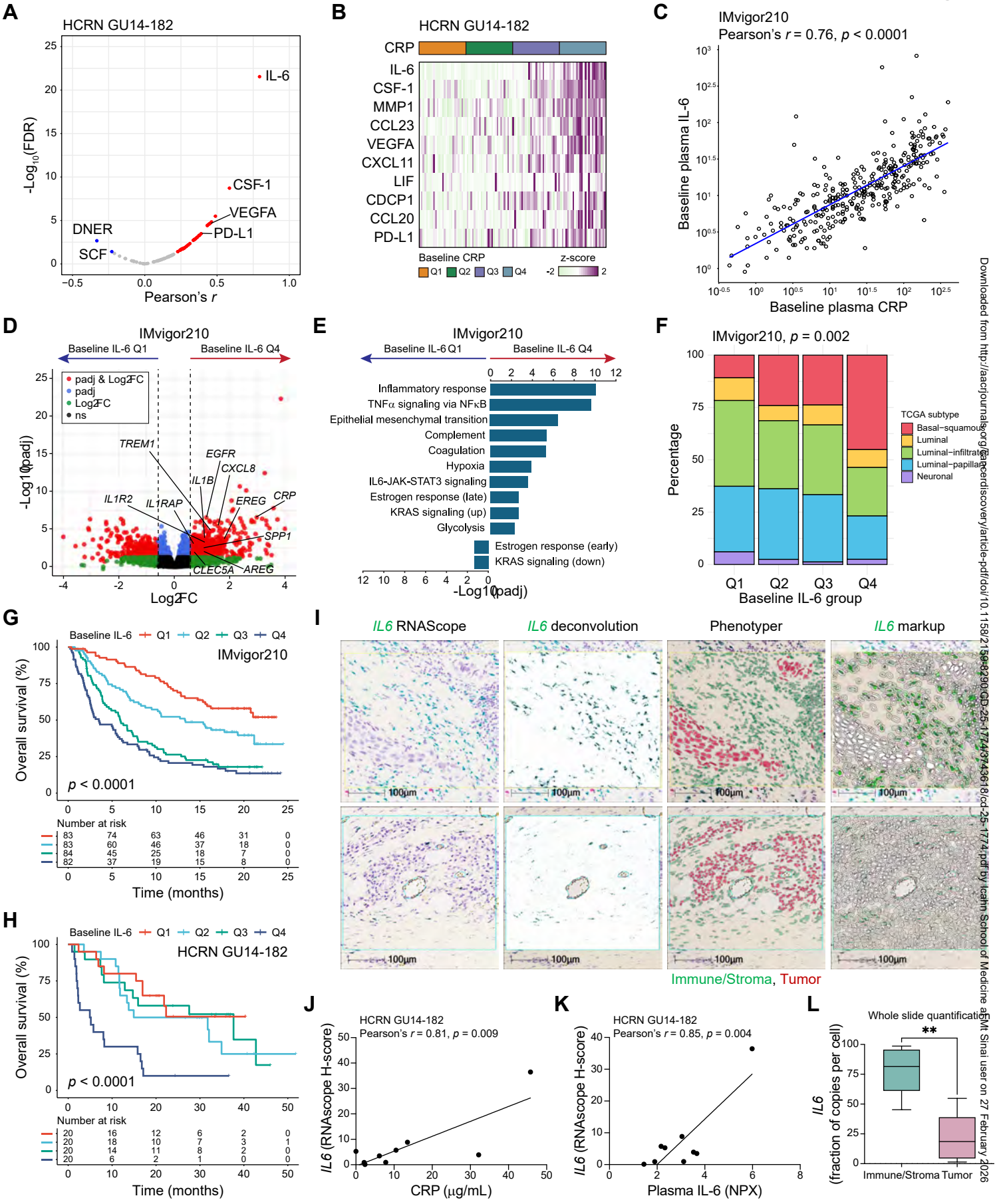

Figure 4

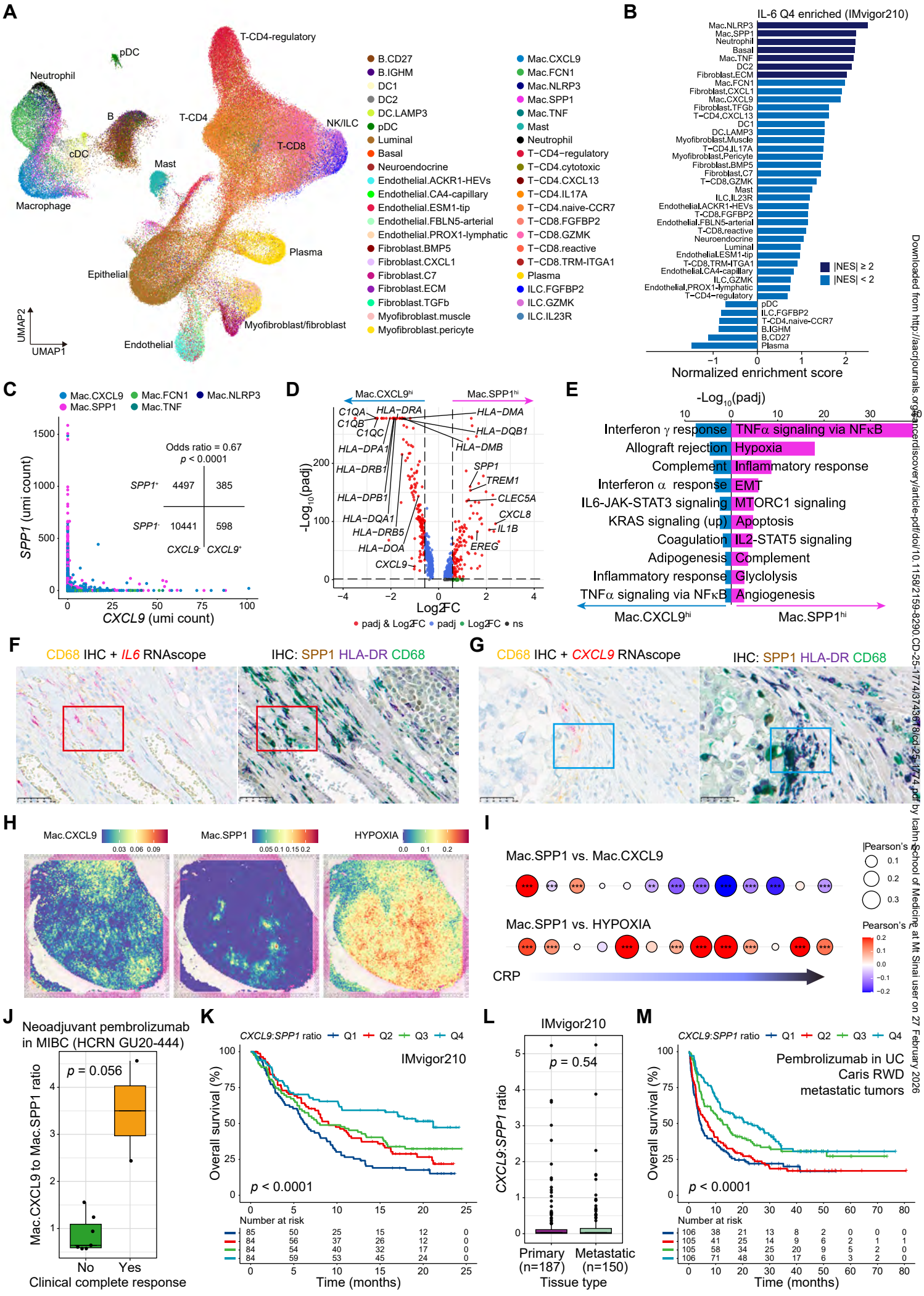

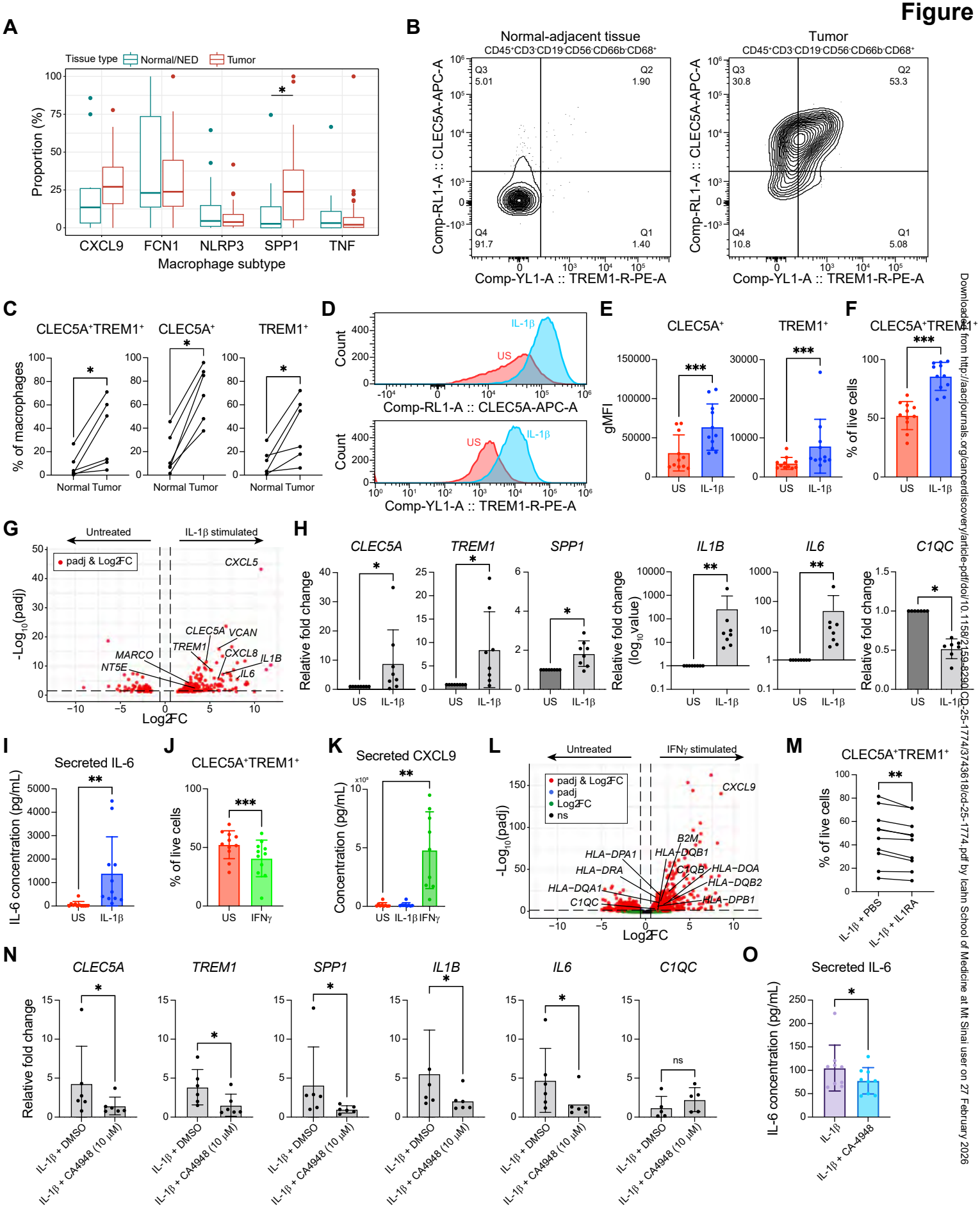

Figure 6

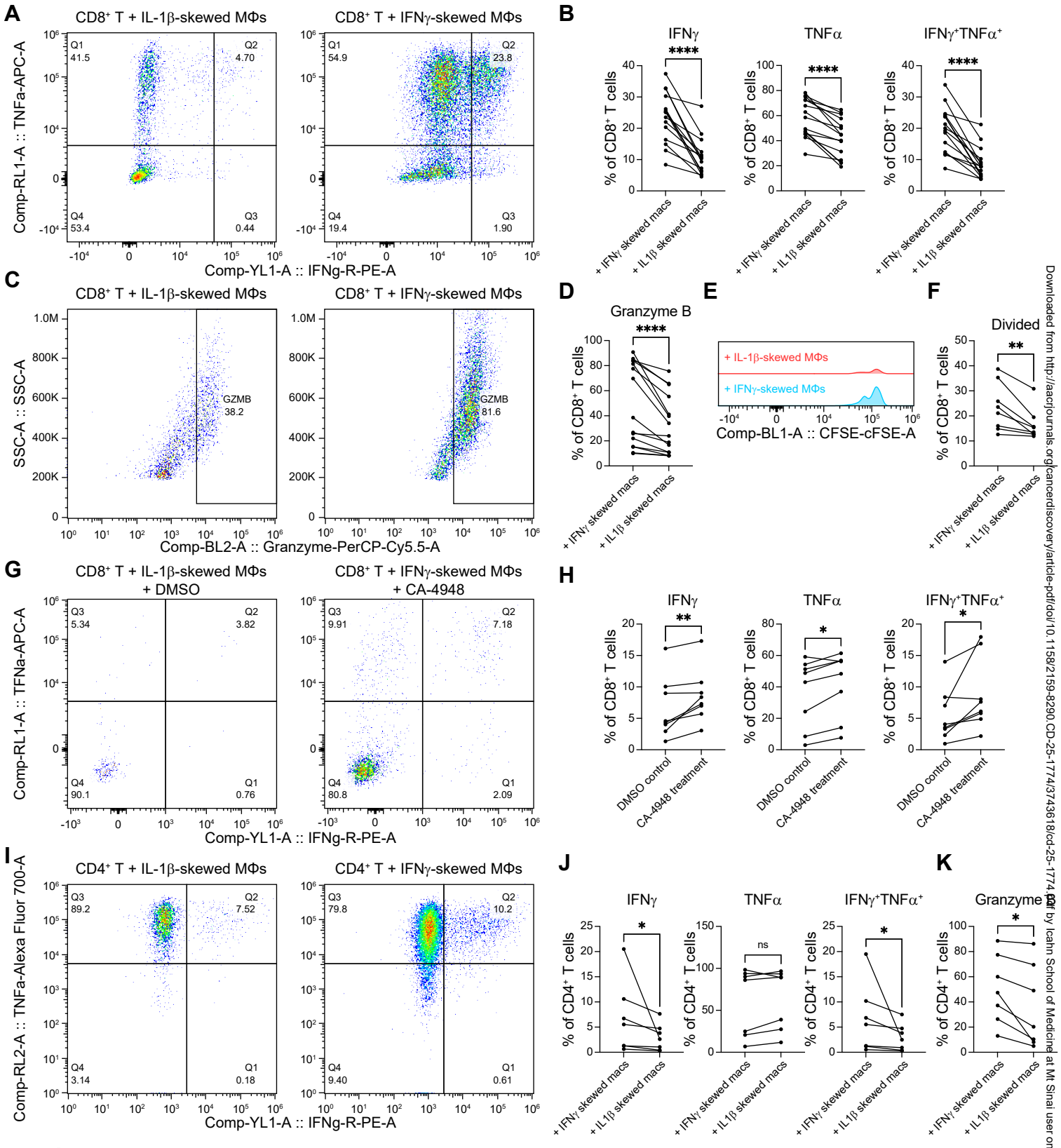

Figure 7